Identification and analysis of nonlinear dynamics of inertial actuators

Mattia Dal Borgo*, Maryam Ghandchi Tehrani and Stephen John Elliott

Signal Processing and Control Group, Institute of Sound and Vibration Research, University of Southampton, Highfield, SO17 1BJ, Southampton, United Kingdom

* Corresponding author. E-mail address: M.Dal-Borgo@soton.ac.uk

Keywords: Electrodynamic inertial actuator; Nonlinear system identification; Non-smooth nonlinearity.

Abstract

This paper presents an experimental study of the nonlinear dynamics of electrodynamic proof mass actuators. When inertial actuators are used in velocity feedback controllers, their nonlinear dynamics can affect the stability margin of the feedback loop. Thus, it is crucial to identify the nonlinearity sources and to build reliable models that can be implemented in the stability analysis. Firstly, the underlying linear model parameters of an inertial actuator are identified for small excitation signals. The inductance losses at high frequencies due to eddy currents have also been included in the electrical impedance model. Secondly, the nonlinear model of the inertial actuator is determined using the detection, characterisation and identification process. Finally, a numerical analysis is carried out to highlight the implications of nonlinear dynamics of inertial actuators. The proposed methodology is applied to several electromagnetic proof mass actuators, including when the proof mass is not accessible to be directly instrumented.

1. Introduction

Extensive research has shown the importance of active devices to control vibrations of lightweight and flexible structures [1-7]. A notable example are velocity feedback controllers, which can add viscous damping to the structure, reducing its level of resonant vibration [5]. A velocity feedback controller consists of an actuator attached to a structure with a collocated sensor of vibration (usually an accelerometer) and a controller, which feeds back the velocity of the structure to the actuator [5]. The use of an electromagnetic inertial, or proof mass, actuator as the active forcing device in velocity feedback controllers has also been well documented [2, 5, 7-14]. An inertial actuator consists of a magnetic proof mass, an electrical winding and a suspension, which connects the proof mass to a casing or base mass [7]. An example of such a device is shown in Figure 1(a) and its schematic representation is displayed in Figure 1(b).

(a) (b)

Figure 1: (a) Picture of the Micromega Dynamics IA-01 inertial actuator; (b) Schematic of an inertial actuator in cross-section.

An inertial actuator operates as a coil-magnet electrodynamic transducer. The control, or secondary, force on the structure is generated by the interaction between the constant magnetic flux of the magnet

and the variable magnetic flux produced by the current flowing through the coil. The transducer supplies the control force on the structure by reacting against the proof mass, which consequently starts to accelerate [7]. Electromagnetic proof mass actuators have a wide variety of applications, among which the most important are: space structures, buildings, bridges and other civil structures, and internal noise reduction in aircrafts [15-18]. A large amount of literature has shown that the internal dynamics of the inertial actuator affect the stability and performance of the controller when implemented for structural vibration reduction [12, 19-21]. This motivates for having an accurate model of the inertial actuator and in particular to look for nonlinearities that may affect the dynamics of such a device for large excitation signals. Most studies in this area have not dealt with accurate nonlinear models of inertial actuators. In fact, there is little published data on the nonlinear behaviour of inertial actuators. To date, Baumann *et al.* [22, 23], Wilmshurst *et al.* [24-26] and Dal Borgo *et al.* [27, 28] have highlighted the implications of their nonlinear dynamics. Although there exists few publications based on experiments [25, 29, 30], a systematic methodology of measuring and identifying the nonlinearity in inertial actuators is still lacking. This study aims to determine the mechanical nonlinearities of inertial actuators through the detection, characterisation and identification of the nonlinear parameters in order to build reliable models. The electrical nonlinearities are neglected since they mainly affect the behaviour at high frequencies, which are beyond the frequency region where the instability of velocity feedback loops with inertial actuators occur. One of the harshest nonlinearity that affects the dynamic behaviour of an inertial actuator is stroke saturation. The displacement saturation phenomenon in inertial actuators has been investigated in [8, 22, 24, 25, 30-32]. We investigate in detail the phenomenon of stroke saturation, and also show the results of the same methodology applied to several actuators with weaker and different kind of nonlinearities

This paper investigates the nonlinear behaviour of inertial actuators and provides a methodology for detection, characterisation and identification of the nonlinear parameters. Initially, the experimental analysis is presented to determine the underlying linear parameters of the inertial actuator, in sections 2 and 3. Secondly, the detection, characterisation and identification of the nonlinearities are presented in sections 4 and 5, where the experimental data is analysed. Finally, a theoretical investigation on the experimentally identified model is reported in section 6. This highlights the implications of the nonlinear behaviour of the inertial actuator for its usefulness in velocity feedback controller through the analysis of nonlinear frequency response curves and frequency-amplitude plots.

2. Experimental set-up

In this section the experimental set-up for the identification of the linear and nonlinear dynamics of an inertial actuator is presented. The inertial actuator initially used in the experiments is a Micromega Dynamics IA-01, which is shown in in Figure 1(a) and is documented in [33]. The methodology used for the identification is explained in detail for this specific actuator. However, the same methodology can be applied for the identification of any other inertial actuator. As evidence, a number of different actuators have been tested and their results are provided in Appendix A and Appendix B. To characterise the inertial actuator, two experiments are required. The first experimental set-up is to measure the structural response of the actuator subject to a base excitation, as shown in Figure 2(a). In this case, the actuator is mounted on a PCB Piezotronics 208C01 ICP force sensor, which is rigidly connected to an LDS V406 electrodynamic shaker. The shaker is powered by an LDS PA25E voltage driven voltage amplifier. A B&K Type 4375 accelerometer is attached to the actuator casing in order to measure the acceleration of the base mass. The actuator's coil terminals are initially left open to measure the voltage due to the back-electromotive force (back-EMF). The output force, acceleration and voltage signals are acquired by a dSpace 1103 control board. The dSpace operates the analogue-to-digital and digital-to-analogue conversions (ADC/DAC) of the input and output singals at a sampling frequency of f_s=10 kHz. The dSpace is also connected to a PC workstation. A model of the experiment is created in Matlab/Simulink in order to generate the adequate input signal and to acquire the signals from the measurement channels. The Simulink model is then implemented in the ControlDesk for communicating with the dSpace board. The driving signal is sent from the dSpace board and low-pass filtered (1 kHz cut-off) by a Kemo VBF8 before entering the PA25E amplifier and then to the shaker. A constant voltage signal input to the amplifier is thus converted to a constant displacement signal input to the shaker moving mass, i.e. to the actuator base mass. The second

experimental set-up is used to measure the mechanical response of the actuator to a current excitation, as shown in Figure 2(b). Since the aim of this experiment is to measure the blocked force, the actuator is fixed to a rigid clamped mass and the force at the base is measured by a PCB 208C01 ICP force cell positioned between the actuator and the blocked mass. In this experiment, the signal generated by the dSpace is low-pass filtered (4 kHz cut-off) and amplified by a Micromega Dynamics PR-052-01-04-03 voltage driven current amplifier [34] before entering the actuator leads. Considering this set-up, a constant voltage signal input from the dSpace to the amplifier is converted to a constant current signal input to the actuator's coil [34]. The amplifier also has an output monitoring port for measuring the current of the load. Again, the current and voltage signals are acquired by the dSpace board at a rate of 10 kHz.

(a) (b)

Figure 2: (a) picture of the set-up for the base excitation experiment; (b) picture of the set-up for the blocked base experiment.

The underlying linear parameters for both tests have been measured by applying a broadband white noise excitation and recording the measurements for 60 seconds and taking averages. For the base blocked experimental set-up the only constraint is that the base mass of the actuator is fixed to the ground. Several other excitations under different constraints have been used for the base excitation experiments. In order to better investigate both the linear and the nonlinear regimes of motion. In particular, for the underlying linear parameters identification, the actuator's coil terminals are firstly left open (zero current circulating) and then shunted (zero voltage across the terminals) in order to see the additional damping introduced by the electromechanical coupling. To identify the nonlinear behaviour, the actuator's coil terminals are left open circuit in order to measure the back-EMF and the excitation is chosen to be initially harmonic to detect any nonlinearities. The investigation is followed by sine-sweep excitation experiments, both up and down, in order to catch all the information about the instantaneous frequencies in the response. In this case the experiment is 60 seconds long for linearly sweeping up (down) from 5 Hz (25 Hz) to 25 Hz (5 Hz) at a rate of 40 Hz/min (-40 Hz/min).

3. Underlying linear parameter identification (small amplitude signals)

The operating principle of an electromagnetic proof mass actuator is to convert electrical power into mechanical power exploiting the Lorentz force law. In such a system, a current flowing through a coil is exposed to a uniform magnetic flux, which is generated by the magnetic proof mass. In order to understand the dynamic behaviour of the electrodynamic proof mass actuator, a two-port network is built for such a system. Two-port networks are often used for electrical circuits, because it is relatively easy to obtain the impedances of the different elements by setting the open-circuit or the short-circuit of each two ports. The equivalent electromechanical linear lumped parameter model of the inertial actuator is shown in Figure 3, where m_b is the base mass of the actuator, while m_p represents the proof mass. x_b and x_p are the base mass and proof mass displacement, respectively. k_p and c_p represent the stiffness and damping of the actuator's suspension. The external force applied to the base for the equilibrium is denoted by f. The variable i_a is the current flowing through the coil, while e_a is the voltage across the coil terminals. The electromechanical coupling factor is Bl, where B is the magnetic flux generated by the permanent magnet and l is the length of the winding exposed to the

magnetic flux B. The voice coil is typically modelled as a series ideal inductance L_e and resistor R_e. This is not entirely true, particularly at high frequencies [35, 36]. In fact, the voice coil is not operating in free air, but close to the magnetic pole structure. Hence, the variable magnetic field generated by the current flowing through the coil induces eddy currents in the solid iron pole structure due to Faraday's law. The eddy currents circulating through the resistance of the iron pole dissipate energy by heating the iron pole itself. In loudspeaker driver investigations, this is commonly taken into account by adding lossy inductors in the model, that are, inductors with a shunting parallel resistance [37-39]. Thus, substituting the inductance L_e displayed in Figure 3 with an electrical circuit that has the topology represented in Figure 20(a) results in the electrical impedance,

$$Z_L(j\omega) = \frac{j\omega L_2 R_2}{j\omega L_2 + R_2}. \tag{1}$$

The model described by equation (1) is usually called LR-2 [38, 39]. For the sake of simplicity, throughout this paper the ideal inductance L_e is used in the model, hence the effect of the eddy currents is neglected. Using the linear lumped parameter model of Figure 3, the equilibrium equations at the mechanical and electrical ports can be written as,

$$\begin{cases} j\omega m_p \dot{X}_p(j\omega) = BlI_a(j\omega) - \left[c_p + \frac{k_p}{j\omega}\right]\dot{X}_r(j\omega) \\ F(j\omega) = BlI_a(j\omega) - \left[c_p + \frac{k_p}{j\omega}\right]\dot{X}_r(j\omega) + j\omega m_b \dot{X}_b(j\omega) \\ E_a(j\omega) = Bl\dot{X}_r(j\omega) + [R_e + j\omega L_e]I_a(j\omega) \end{cases}. \tag{2}$$

The transformation in frequency domain is carried out considering the linearity assumption and using the notation of capital letters for variables in frequency domain. Also, in equation (2) the relative velocity between the proof mass and the base mass is written as $\dot{X}_r(j\omega)$. All the properties of the electromechanical interaction are well described by six FRFs. These are the transmissibility between the two ports and the driving-point impedances of the inertial actuator at either its electrical or mechanical terminals.

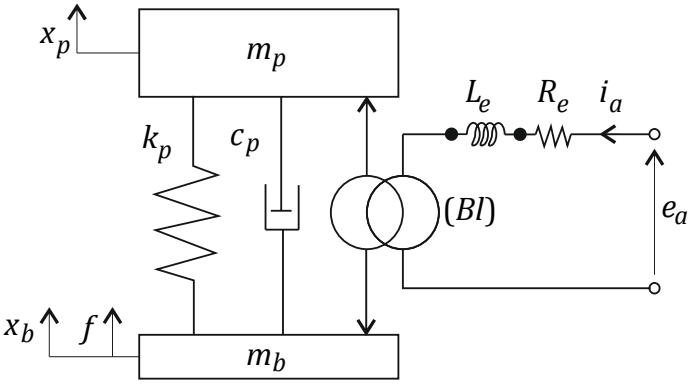

Figure 3: Linear lumped parameter model of the proof mass actuator.

The full mathematical derivation of these FRFs is described in the textbooks of Hunt [40] and Crandall [41]. Here, the well-known resulting formulation is reported. The electric driving-point impedance $Z_{ee}(j\omega)$ is defined as the ratio between the voltage at the coil terminals and the current flowing through the coil, when the base mass is blocked ($\dot{X}_b(j\omega) = 0$). Hence, from the equations in (2) the electric impedance can be written as,

$$Z_{ee}(j\omega) = \left.\frac{E_a(j\omega)}{I_a(j\omega)}\right|_{\dot{X}_b(j\omega)=0} = (R_e + j\omega L_e) + \frac{(Bl)^2}{j\omega m_p + c_p + \frac{k_p}{j\omega}}. \tag{3}$$

Similarly, the mechanical driving-point impedance $Z_{mm}(j\omega)$ is defined as the ratio between the transmitted force to the hosting structure and the velocity of the base mass. Considering equation (2), if the electrical port is opened ($I_a(j\omega) = 0$), the open-circuit mechanical impedance $Z_{mm,o}(j\omega)$ can be obtained as,

$$Z_{mm,o}(j\omega) = \frac{F(j\omega)}{\dot{X}_b(j\omega)}\Big|_{I_a(j\omega)=0} = j\omega m_b + \frac{j\omega m_p\left(c_p+\frac{k_p}{j\omega}\right)}{j\omega m_p+c_p+\frac{k_p}{j\omega}} \ . \tag{4}$$

The mechanical impedance can also be calculated in shunted electrical port scenario ($E_a(j\omega) = 0$). In this case, from equation (2) the shunt-circuit mechanical impedance $Z_{mm,s}(j\omega)$ can be written as,

$$Z_{mm,s}(j\omega) = \frac{F(j\omega)}{\dot{X}_b(j\omega)}\Big|_{E_a(j\omega)=0} = j\omega m_b + \frac{j\omega m_p\left(c_p+\frac{k_p}{j\omega}+\frac{(Bl)^2}{R_e+j\omega L_e}\right)}{j\omega m_p+c_p+\frac{k_p}{j\omega}+\frac{(Bl)^2}{R_e+j\omega L_e}} \ . \tag{5}$$

The transmissibility between the two ports during the base excitation experiment is defined as the ratio between the voltage across the coil terminals and the velocity of the base mass, when the electrical port is opened ($I_a(j\omega) = 0$). Hence, from equation (2) the transmissibility can be written as,

$$T_{\dot{X}_b}(j\omega) = \frac{E_a(j\omega)}{\dot{X}_b(j\omega)}\Big|_{I_a(j\omega)=0} = \frac{-j\omega m_p(Bl)}{j\omega m_p+c_p+\frac{k_p}{j\omega}} \ , \tag{6}$$

The transmissibility for the base blocked experiment is defined as the ratio between the force transmitted to the hosting structure and the input current, when the base mass is blocked ($\dot{X}_b(j\omega) = 0$). For this reason, it is also called actuator's blocked force. Again, from equation (2), the transmissibility can be written as,

$$T_{I_a}(j\omega) = \frac{F(j\omega)}{I_a(j\omega)}\Big|_{\dot{X}_b(j\omega)=0} = \frac{-j\omega m_p(Bl)}{j\omega m_p+c_p+\frac{k_p}{j\omega}} \ , \tag{7}$$

Similarly, the transmissibility can be calculated with respect to the input voltage in the same blocked base mass configuration. In this case, from equation (2) it follows that,

$$T_{E_a}(j\omega) = \frac{F(j\omega)}{E_a(j\omega)}\Big|_{\dot{X}_b(j\omega)=0} = \frac{1}{(R_e+j\omega L_e)}\frac{-j\omega m_p(Bl)}{\left(j\omega m_p+c_p+\frac{k_p}{j\omega}+\frac{(Bl)^2}{R_e+j\omega L_e}\right)} \ , \tag{8}$$

During the experiments, all these FRFs have been measured using a broadband white noise excitation. In particular, $Z_{mm,o}(j\omega)$, $Z_{mm,s}(j\omega)$ and $T_{\dot{X}_b}(j\omega)$ have been measured using the base excitation set-up, while $Z_{ee}(j\omega)$, $T_{I_a}(j\omega)$, $T_{E_a}(j\omega)$ have been measured using the blocked base testing set-up. The experimental results together with the linear model identification are shown in Figure 4, Figure 5, Figure 6, where the magnitude, phase and coherence are displayed for each measured FRF. The FRFs plotted with the black solid line are the averages of eight measurements, each one of 60 seconds long. The measured FRFs have been fitted with the analytical FRFs given by equations (3), (4), (5), (6), (7) and (8),which are shown in the figures with the blue dashed lines. A least-square-error method has been implemented for the linear model identification of the best parameters, which are summarised in Table 1. There is a very good agreement between the experimental and the analytical FRFs above 5 Hz, except for the electric impedance in Figure 6(b). As explained before, due to the inductance losses the experimental FRF does not follow the purely inductive behaviour. In fact, the magnitude of the electrical impedance rises with respect to the frequency with a slope that is lower than 20 dB per decade. This is confirmed by looking at the phase plot of Figure 6(b), where the phase does not reach the 90 degrees given by the inductive behaviour, but it stays somewhere in the middle between 0 and 90 degrees. The inductance losses have been modelled using the Leach model [42] in Appendix C given by equation (C3). The analytical electric impedance including the Leach model has been fitted to the measured electric impedance in order to obtain the model parameters. The result of the fitting is shown in Figure 6(b) with the red dotted line using the identified coefficients of the fitted Leach model

that are $K = 4.5 \cdot 10^{-4}$ and $n = 0.85$. It is evident that including the inductance losses in the model will give a better prediction of the electrical impedance.

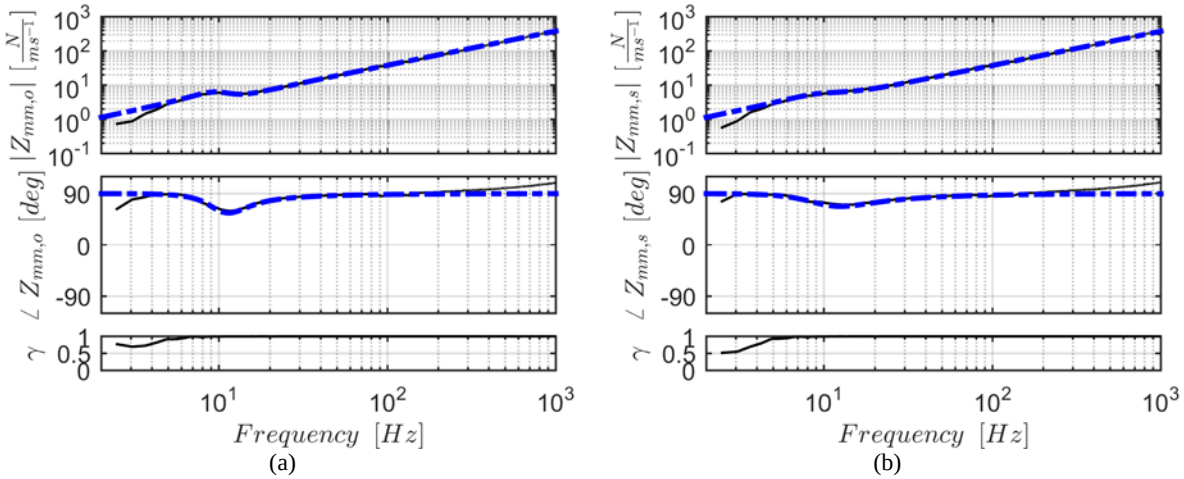

(a) (b)

Figure 4: Magnitude, phase and coherence of the measured mechanical impedance (black solid line) and identified model (blue dashed line): (a) open circuit configuration; (b) shunted circuit configuration.

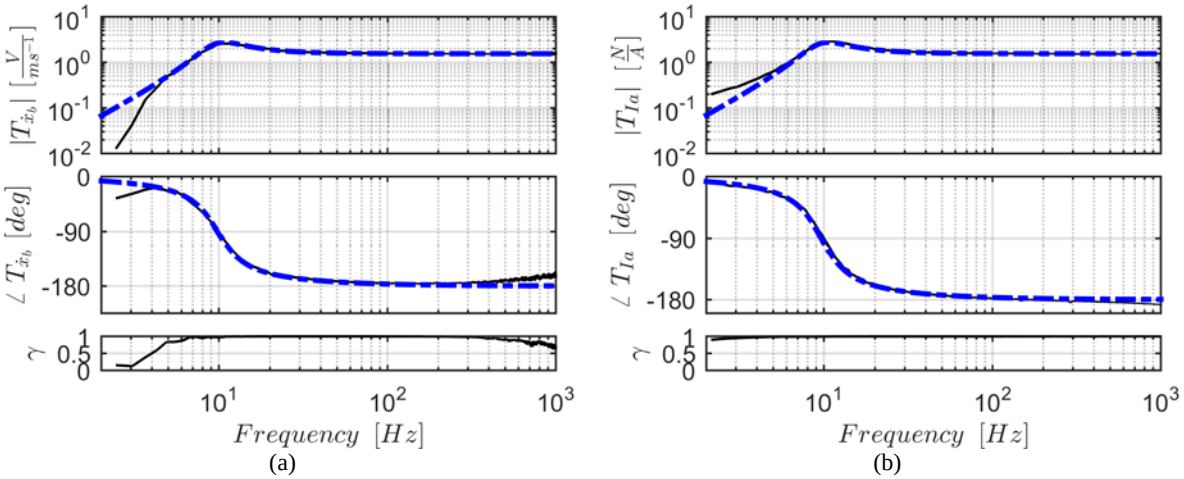

(a) (b)

Figure 5: Magnitude, phase and coherence of the measured transmissibility (black solid line) and identified model (blue dashed line): (a) base excitation experiment; (b) base blocked current excitation experiment.

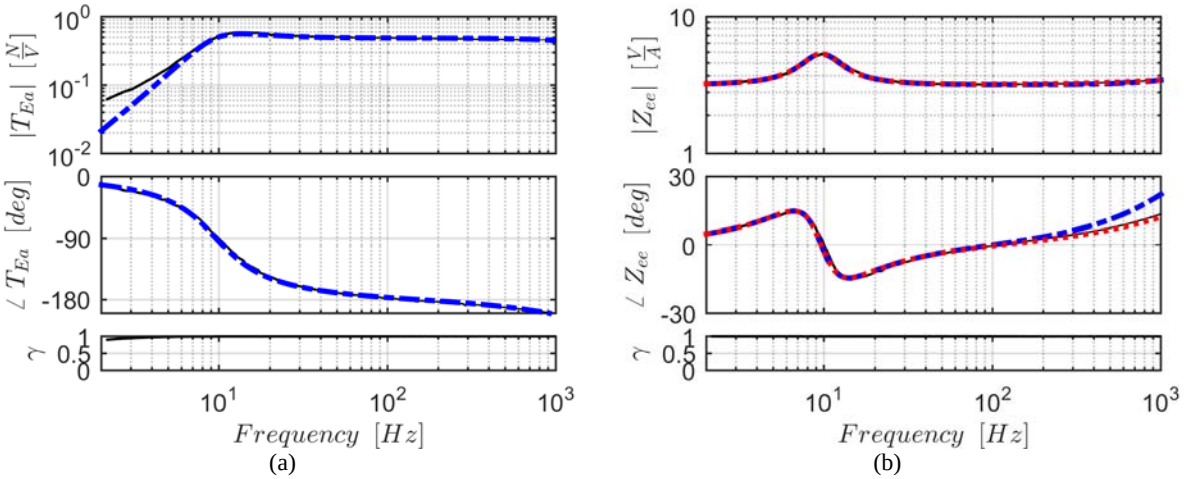

(a) (b)

Figure 6: Magnitude, phase and coherence of the measured transmissibility and electric impedance (black solid line) and identified model (blue dashed line): (a) transmissibility of the base blocked voltage excitation experiment; (b) electric impedance considering an ideal inductance model (blue dashed line) and a Leach model (red dotted line).

Table 1: Identified actuator linear model parameters.

Parameter	Base mass	Proof mass	Transduction coefficient	Natural frequency	Damping ratio	Coil resistance	Coil inductance
Symbol	m_b	m_p	Bl	ω_p	ζ_p	R_e	L_e
Value	0.054	0.031	1.55	9.7	30%	3.2	211
Units	kg	kg	N/A	Hz	-	Ω	μH

4. Limits of linear analysis

The dynamic behaviour of inertial actuators is not always well described by linear mathematical models. There are strong nonlinearities due to a harsh change in the dynamic behaviour of the actuator. These harsh nonlinearities are due to the saturation of the force generated by the actuator due to the saturation of the power electronics and due to the saturation of the maximum displacement allowed to the proof mass. Considering the blocked base mass configuration, from equation (2) it follows that the blocked force can be written as,

$$F_b(j\omega) = \begin{cases} -[j\omega c_p + k_p]X_p(j\omega) + BlI_a(j\omega) & \text{(9a)} \\ \omega^2 m_p X_p(j\omega) & \text{(9b)} \end{cases}$$

considering the equation of motion of the proof mass and substituting into equation (9a), the maximum force that the actuator can deliver without exceeding the limits is given by,

$$F_{b,max}(j\omega) = \begin{cases} F_{b,max1}(j\omega) = F_{a,max}(j\omega)\left(\frac{\omega^2}{-\omega^2 + j\omega 2\zeta_p\omega_p + \omega_p^2}\right), & \text{(10a)} \\ F_{b,max2}(j\omega) = \omega^2 m_p x_0 & \text{(10b)} \end{cases}$$

where the natural frequency is $\omega_p = \sqrt{k_p/m_p}$ and the damping ratio is $\zeta_p = c_p/(2m_p\omega_p)$. $F_{b,max1}(j\omega)$ and $F_{b,max2}(j\omega)$ represent the force saturation due to the power electronic saturation and the stroke saturation, respectively. The power electronic saturation gives a limitation on the electromechanical conversion, which is given by the maximum actuation force $F_{a,max}(j\omega)$ as,

$$F_{a,max}(j\omega) = (Bl)I_{a,max}(j\omega) \quad (11)$$

where $I_{a,max}(j\omega)$ is the maximum input current to the actuator coil. The stroke saturation gives a limitation on the maximum displacement achievable for the proof mass. This is given by,

$$X_{p,max}(j\omega) = x_0 \quad (12)$$

where x_0 is half of the stroke length. The results of this analysis are shown in Figure 7(a) for the Micromega Dynamics IA-01 inertial actuator driven by a current amplifier. The dotted and dash-dotted blue lines in Figure 7(a) show in a logarithmic scale the spectrum of the actuation force $F_{a,max}(j\omega)$ and the blocked force $F_{b,max1}(j\omega)$, when the actuator is driven by the maximum current of 1 A. The dashed red line shows instead the spectrum of the blocked force $F_{b,max2}(j\omega)$, when the actuator is driven at the maximum stroke of the proof mass ($x_0 = 1.25\ mm$).

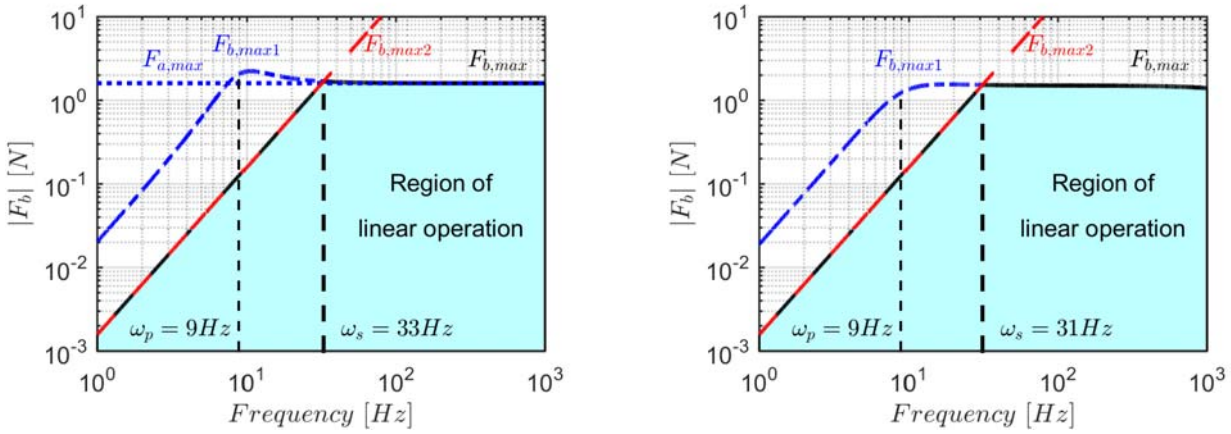

Figure 7: Limitation of the linear analysis for a proof mass actuator. Dotted and dash-dotted blue lines represent the limitation on the maximum force due to saturation of the power electronics; red dashed line displays the limitation due to the maximum stroke available; black solid line is the combination of the two previous constraints and gives a limit on the region of linear operation of the inertial actuator (cyan area). (a) Current driven actuator; (b) Voltage driven actuator.

A combination of these two limitations results in a region of linear operation for the inertial actuator, which is defined by the black solid line. The upper limit for the input current, whose dynamics are flat over the frequency range, is indeed a limitation on the temperature and heating of the actuator. As it is well described in [43, 44], an increase in the input power to the actuator's coil would produce a temperature rise of its components. The force limit due to stroke saturation shown in Figure 7(a) appears to be an effective limit at low frequencies, instead. The plot of Figure 7(a) can thus be divided in two regions: below the saturation cut off frequency ω_s, where the limitation of the blocked force is given by stroke saturation; and above the saturation cut off frequency, where the limit is given by the power electronics. One can replicate the same analysis for a voltage driven actuator, setting the limitation of the power electronics on the voltage instead of on the current. This results in,

$$F_{b,max}(j\omega) = \begin{cases} F_{b,max1}(j\omega) = E_{a,max}\left(\dfrac{-j\omega m_p(Bl)}{(R+j\omega L)\left(j\omega m_p + c_p + \frac{k_p}{j\omega} + \frac{(Bl)^2}{R+j\omega L}\right)}\right), & \text{(13a)} \\ F_{b,max2}(j\omega) = \omega^2 m_p x_0 & \text{(13b)} \end{cases}$$

where $E_{a,max}$ is the maximum voltage that can be applied to the actuator voice coil. The limits given by equations (13a,b) are shown in Figure 7(b), where the maximum voltage has been set to 3 V. Stroke saturation can happen to every inertial actuator if excited below its saturation cut-off frequency ω_s (e.g. the Fraunhofer LBF prototype actuator in Appendix A). In fact, in a real application, inertial actuators are subject to shocks, rigid body motions or other low frequency excitations that can lead to stroke saturation. This is outside the working range of inertial actuators and designing an actuator that is able to deliver the requested force even below the saturation cut-off would mean that it is overdesigned in terms of volume and weight. This would negate its favourable force to weight ratio for controlling vibrations of lightweight structures.

5. Nonlinear parameter identification (large amplitude signals)

In general, the assumption of linearity in the model holds only for small amplitude signals. For large amplitude signals, a nonlinear model of the inertial actuator is required to reliably predict the behaviour of the actuator. This is crucial in case of instabilities or large amplitude of motions. A nonlinear lumped parameter model of the inertial actuator is shown in Figure 8.

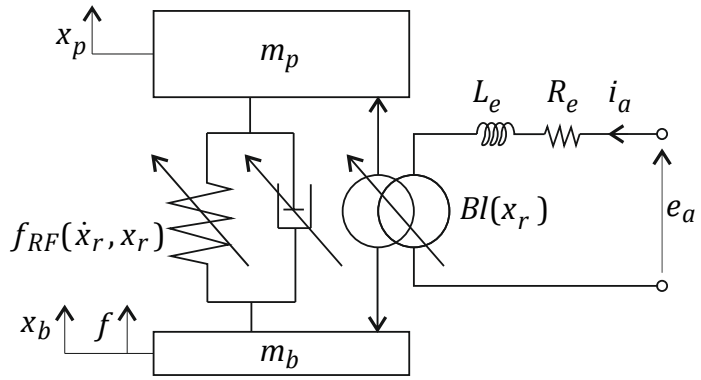

Figure 8: Lumped parameter model of the proof mass actuator considering a nonlinear connection between the two masses and a nonlinear transduction.

In this figure, the linear parameters describing the suspension have been replaced by a nonlinear restoring force $f_{RF}(\dot{x}_r, x_r)$. Also, the transduction factor is in general a nonlinear function of the displacement. Only mechanical nonlinearities are considered, which depend on displacements or velocities. The electrical nonlinearities, which depend on the current or voltage are neglected since they affect the behaviour at high frequencies. The governing equations of the system in Figure 8 can be written as,

$$\begin{cases} m_p\ddot{x}_p(t) = -f_{RF}\big(\dot{x}_r(t), x_r(t)\big) + Bl\big(x_r(t)\big)i_a(t) \\ f(t) = Bl\big(x_r(t)\big)i_a(t) - f_{RF}(\dot{x}_r(t), x_r(t)) + m_b\ddot{x}_b(t) \\ e_a(t) = Bl\big(x_r(t)\big)\dot{x}_r + R_e i_a(t) + L_e \frac{\mathrm{d}}{\mathrm{dt}} i_a(t) \end{cases}, \tag{14}$$

where the transformation to the frequency domain is not generally possible due to the nonlinear nature of these equations. The nonlinearity of the inertial actuator is identified following three steps, namely detection, characterisation and parameter identification, as proposed in [45, 46]. The inertial actuator is again tested using the base excitation experiment described in section 2. The first test is a harmonic excitation at different frequencies. This is useful to detect the nonlinearities by comparing the excitation and response waveforms and looking for distortions. If a nonlinear behaviour has been detected, a different type of excitation is applied to the inertial actuator in order to characterise the nonlinearity. This is done using linear sine sweep up and down excitations. Looking at the time history of the response and at the instantaneous frequencies, a formulation can be chosen for the nonlinear model. Finally, the nonlinear model parameters can be identified using the restoring force surface method [45-49].

5.1. Detection

In this section the detection of the nonlinearity is investigated. Several experiments have been done using a harmonic excitation and varying frequency and amplitude of excitation. The most representative is shown in Figure 9 for a harmonic excitation at 8 Hz. In particular, Figure 9(a) shows the waveforms of the base force, the relative velocity and the displacement of the proof mass. The waveform of the base force presents periodic spikes, which are due to the impacts between the proof mass and the casing. In fact, at the same location of the spikes, the velocity plummets changing sign, and the displacement clips resulting in a highly distorted waveform. The distorted waveforms results in a distorted trajectory of the proof mass in the phase-space, as shown in Figure 9(b). If the system were linear the trajectory would have been elliptical, in this case instead it follows a distorted loop constrained within a certain displacement range. In Figure 9(c) the waveform of the back-electromotive force (back-EMF) is shown. This signal is also highly distorted and its waveform is similar to the waveform of the proof mass velocity in Figure 9(a). Figure 9(d) shows the power spectral densities of the proof mass displacement and the back-EMF. It can be seen that many harmonics are generated and their magnitudes are comparable to the fundamental.

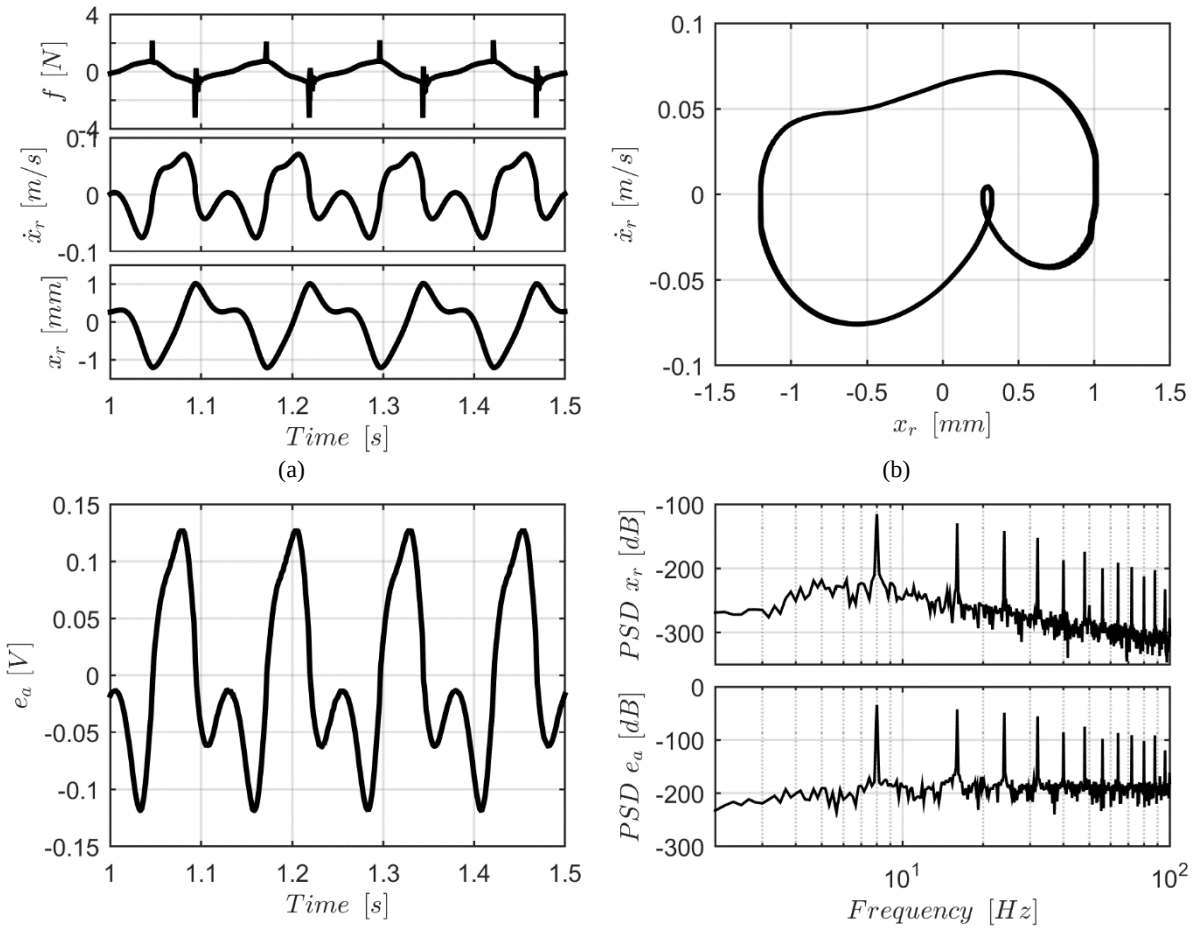

Figure 9: Detection of the nonlinearity with a harmonic excitation at 8 Hz; (a) waveforms of the base force, relative velocity and displacement of the proof mass; (b) phase space trajectory of the proof mass; (c) waveforms of the back EMF; (d) power spectral densities (PSDs) of the relative displacement and voltage..

The relevance of the harmonics generated by the nonlinearity, or the magnitude of waveform distortion is analysed considering the Total Harmonic Distortion (THD) of the signals [50], which is defined as,

$$THD = \frac{\sqrt{\sum_{n=2}^{\infty} I_n^2}}{I_1}, \tag{15}$$

where I_1 is the magnitude of the fundamental frequency in the response, and I_n are the harmonics. The THD of the signals in Figure 9 are given in Table 2 considering the harmonics up to the 5th. The THD is usually given in dBc (dB relative to the carrier), but it can be easily translated in percentage.

Table 2: Total Harmonic Distortion of displacement, force and voltage signal at 8 Hz harmonic excitation considering up to the 5th harmonic.

Parameter	$THD\ x_r$	$THD\ x_r$	$THD\ f$	$THD\ f$	$THD\ e_a$	$THD\ e_a$
Value	-6	50	-2.8	72.2	-2.2	77.2
Units	dBc	%	dBc	%	dBc	%

The results shown in Figure 9 and Table 2 motivates for a deeper understanding of the causes of the nonlinearity as well as the identification of the nonlinear actuator model.

5.2. Characterisation

In this section the characterisation of the nonlinearity is investigated. Several experiments have been carried out using a sine sweep excitation and varying amplitude of excitation. The first test was to compare the sweep-up excitation to the sweep-down excitation in order to check for hardening or softening behaviour of the spring. The results for an amplitude excitation of 0.65 mm for the base mass displacement are presented in Figure 10. The sweep-up time history is shown with the black line, whereas the sweep-down is shown with the grey line. The response to the sweep-up excitation from 5 Hz to 25 Hz at 40 Hz/min is characterised at low frequencies by a limitation on the displacement. The amplitude response remains close to the saturation level until the excitation reaches 20 Hz, then a sudden jump down to a lower amplitude level can be observed. This nonlinear effect is referred to as the jump phenomenon and is peculiar of systems with hardening stiffness nonlinearities [45, 46, 49]. For frequencies higher than the jump, the response amplitude decreases proportionally to the inverse of the frequency. The sweep down response in Figure 10 presents a similar behaviour, but the amplitude jump occurs at a lower frequency than the sweep-up. In this case the jump is from a lower amplitude up to a higher amplitude, as the plot to the sweep-down response should be read from right to left. This confirms that the actuator being investigated is characterised by a hardening stiffness behaviour. Another analysis is done to compare the responses to a sweep-up excitation from 5 Hz to 25 Hz at 40 Hz/min at different amplitudes of excitation. The response to the highest level of excitation (x_b =0.65 mm) has been compared to the scaled response at the lowest level of excitation (x_b =0.10 mm). It is noted that the two responses are completely different. In fact, the response at high excitation amplitude presents the nonlinear behaviour with the jump phenomenon described before. The response at low excitation amplitude instead is characterised by a response with an envelope that is a linear FRF. This shows that the resonance frequency of the inertial actuator shifts to higher frequencies as the excitation level increases.

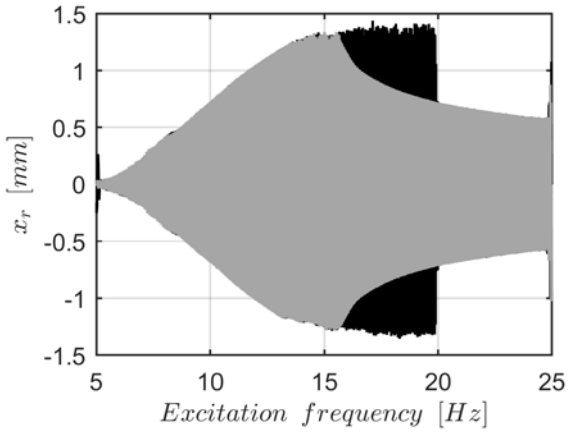

Figure 10: Time history of the relative proof mass displacement due to a sine sweep excitation for an excitation amplitude of 0.65 mm for the base mass displacement; the sweep-up response is shown with the black line from 5 Hz to 25 Hz at 40 Hz/min, the sweep-down response is displayed with the grey line from 25 Hz to 5 Hz at -40 Hz/min.

The sine sweep signals can be further analysed in frequency domain. Classical Fourier transform cannot be applied for this analysis, as the response is nonlinear and the Fourier transform fails to capture time-varying frequencies. The wavelet transform (WT) instead, permits an interpretation of the harmonic components generated by the nonlinearity by mapping the time series to a time-frequency representation. The WT of a signal is defined as,

$$X_r(a,b) = \frac{1}{\sqrt{a}} \int_{-\infty}^{\infty} x_r(t) \psi\left(\frac{t-b}{a}\right) \mathrm{d}t, \tag{16}$$

where $X_r(a,b)$ is the time-frequency representation of the signal, in which the time lies along the x axis and the instantaneous frequency on the y axis. Hence, the variable b locates the observation

window in the time domain, whereas a defines the frequency resolution by expanding or contracting the window. The function $\psi(\cdot)$, namely the mother wavelet, is the windowing function. The wavelet analysis is performed using the NI2D toolbox developed by NOLISYS at the University of Liege (Belgium) [51], which involves a Morlet mother wavelet of the type,

$$\psi(t) = e^{\frac{t^2}{2}} e^{j\omega t}, \tag{17}$$

which is a Gaussian-windowed complex sinusoid. The amplitude of the wavelet transform of the relative displacement for the sweep-up at both the lowest and highest amplitude excitation are shown in Figure 11(a,b). These plots are the amplitude of the instantaneous frequency of the response (y-axis) during the time of the sine sweep excitation (x-axis). Since there is a linear relationship between the time and the frequency of the sine-sweep, the x-axis has been conveniently converted to show the excitation frequency.

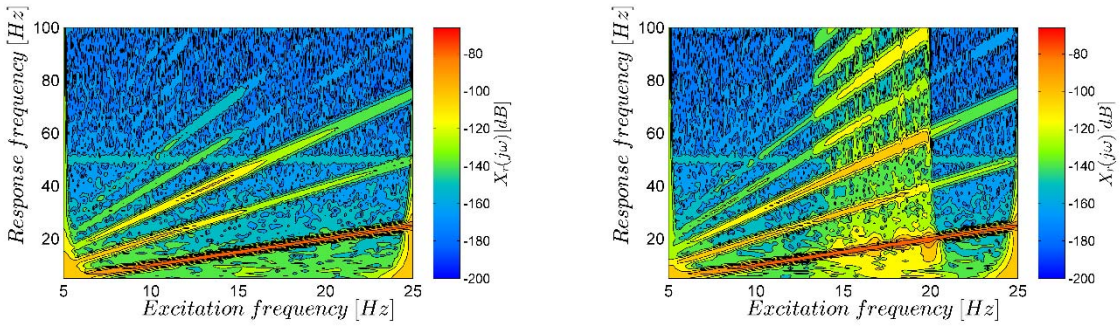

(a) (b)

Figure 11: Amplitude of the wavelet transform of the relative displacement due to a sine sweep-up excitation from 5Hz to 25 Hz at a rate of 40 Hz/min. (a) for an excitation amplitude x_b = 0.10 mm; (b) for an excitation amplitude x_b =0.65 mm

Figure 11(a) shows the amplitude of the WT at low excitation level. The response is characterised by a strong presence of the fundamental frequency, but also by a contribution of the second and third harmonics. This is particularly true at frequencies between 8 and 15 Hz, where the system is close to resonance and experiences a larger amplitude motion. Thus, the model of the suspension should be a polynomial of the 3rd order. Increasing the level of the excitation drives the actuator into stroke saturation, hence experiencing a stronger nonlinearity. The amplitude of the WT at high amplitude is shown in Figure 11(b). The response is characterised by a wideband frequency components, which indicates the presence of non-smooth nonlinearity. This harsh nonlinearity can be modelled using a piecewise function. It can be seen in Figure 11(b) that the response is dominated by the fundamental frequency component for frequencies above the jump phenomenon at 20 Hz.

5.3. Identification

In this section, the identification of the nonlinear parameters is carried out. For this purpose the sine sweep experiments are used and the data is processed using the restoring force method. Figure 12 shows the experimental data points of the restoring force in the phase space for the largest amplitude of excitation. It can be seen that the restoring force measurements are close to a linear behaviour until the actuator reaches the end stops. The restoring force suddenly steepens if the proof mass collides with the end stops. Moreover, the velocity quickly changes sign during stroke saturation and the proof mass can experience multiple impacts as shown in Figure 12 (double impact). In order to identify the nonlinear parameters of the nonlinear function, an assumption is made, which is

$$f_{RF}(\dot{x}_r, x_r) = f_{RF,v}(\dot{x}_r) + f_{RF,d}(x_r), \tag{18}$$

hence, the contribution of the damping and elastic restoring forces can be separated. Assuming equation (18) means that the elastic restoring force can be represented as a section of the plot of Figure 12 at velocities close to zero. The same for the damping restoring force, where a section of Figure 12 at displacements close to zero can be taken.

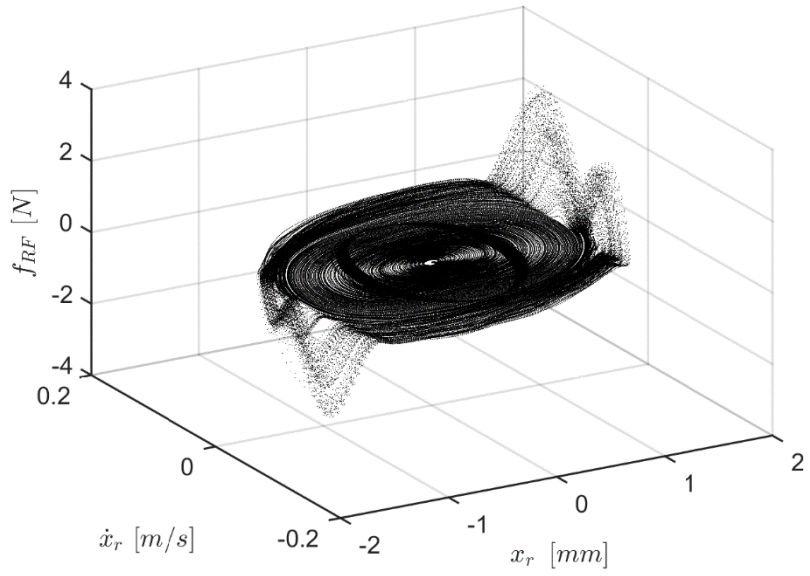

Figure 12: 3D restoring force data points of a sine sweep-up excitation in the phase space.

The scattered data plot of the measured elastic restoring force is shown in Figure 13 with the black dots. It can be seen that the behaviour of the elastic restoring force is polynomial of the 3rd order until the proof mass reaches the end stops. The stroke saturation can be modelled as a non-smooth function with a very large stiffness. From this scattered data plot a nonlinear model can be fitted, which is piecewise for the stroke limit and is polynomial of the 3rd order for the suspension. The fitted model is shown in Figure 13 with the cyan dashed line. A simpler model can also be fitted to the measurements, which is piecewise linear and is shown in Figure 13 with the red solid line. The piecewise linear model is simpler than the polynomial cubic and can still consider the stroke saturation phenomenon. This can be beneficial since the behaviour of the system is affected by the stroke limitation more than the suspension nonlinearity.

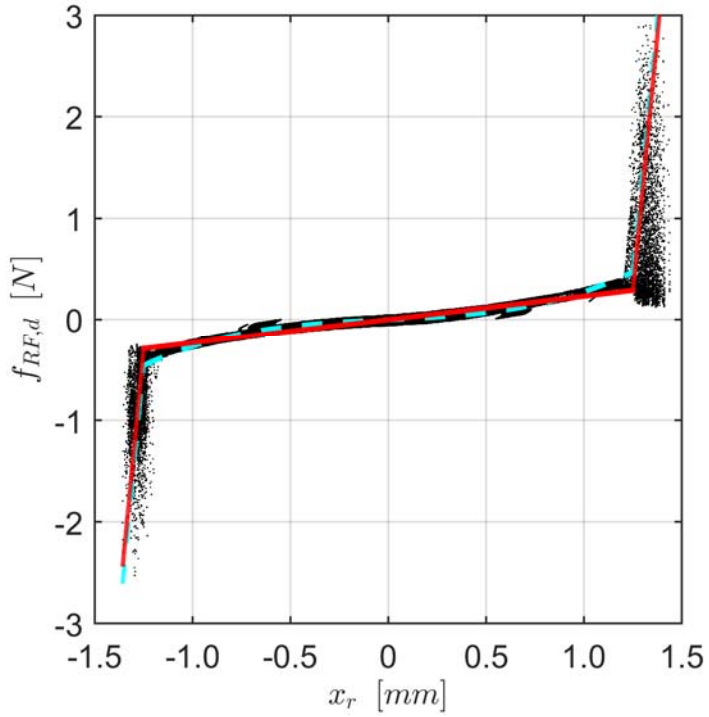

Figure 13: Model identification of the elastic restoring force; experimental data (black dots); fitted cubic stiffness model with saturation (cyan dashed line); fitted piecewise linear model (red solid line).

The elastic restoring force of the fitted polynomial model shown in Figure 13 with the red solid line can be written as,

$$f_{RF,d}(x_r) = \begin{cases} k_{sat}(x_r + x_0) - p_1 x_0^3 + p_2 x_0^2 - p_3 x_0 + p_4 & x_r \le -x_0 \\ p_1 x_r^3 + p_2 x_r^2 + p_3 x_r + p_4 & |x_r| < x_0, \\ k_{sat}(x_r - x_0) + p_1 x_0^3 + p_2 x_0^2 + p_3 x_0 + p_4 & x_r \ge x_0 \end{cases} \quad (19)$$

where the parameters appearing in equation (19) are given in Table 3.

Table 3: Nonlinear model parameters of the elastic restoring force with 3rd order polynomial stiffness between end stops.

Parameter	p_1	p_2	p_3	p_4	k_{sat}	x_0
Value	178000	4450	94	0	20000	1.25
Units	kN/m^3	N/m^2	N/m	N	N/m	mm

If the piecewise linear model were fitted to the data instead of the polynomial cubic one, the elastic restoring force of the fitted model shown in Figure 13 with the cyan dashed line can be written as,

$$f_{RF,d}(x_r) = \begin{cases} k_{sat}(x_r + x_0) - p_1 x_0 + p_2 & x_r \le -x_0 \\ p_1 x_r + p_2 & |x_r| < x_0, \\ k_{sat}(x_r - x_0) + p_1 x_0 + p_2 & x_r \ge x_0 \end{cases} \quad (20)$$

where the parameters appearing in equation (20) are $p_1 = 230\ N/m$, $p_2 = 0\ N$, $k_{sat} = 2 \cdot 10^4\ N/m$ and $x_0 = 1.25\ mm$. It should be noticed that the end stops in Figure 13 are represented by tilted lines instead of vertical lines. This is because the experimental data describes the end stops with a finite stiffness. The two end stops have been found to have slightly different stiffness coefficients. For the sake of simplicity, the mean value of the two has been considered for both end stops.

The scattered data plot of the damping restoring force is shown in Figure 14. It is observed that the experimental data points of the damping restoring force are well fitted by a linear model. The fitted model is shown in Figure 14 with a red solid line and can be written as,

$$f_{RF,v}(\dot{x}_r) = p_1 \dot{x}_r + p_2, \tag{21}$$

where the parameters appearing in equation (21) are $p_1 = 1.4\ N/ms^{-1}$ and $p_2 = 0\ N$.

.

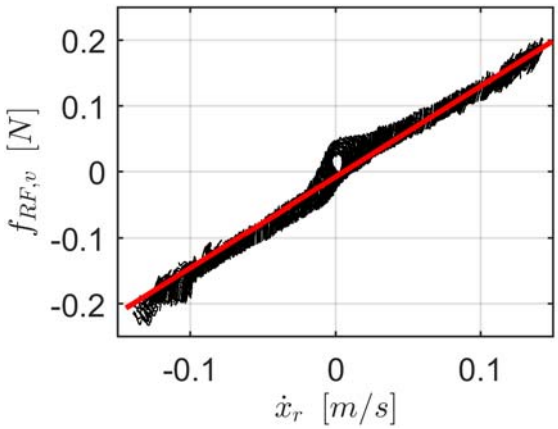

Figure 14: Model identification of the damping restoring force; experimental data (black dots); fitted curve (red solid line).

The scattered data plot of the transduction factor versus the displacement is shown in Figure 15. It can be seen that the behaviour of the transduction coupling is polynomial and symmetric. In fact, the peak in the transduction coupling is reached for the proof mass in centred position. Moving away from the resting position leads to a slight decrease of the transduction coupling factor. From this scattered data plot a nonlinear model can be fitted, which is polynomial of the 2nd order. The fitted model is shown in Figure 15 with a red solid line.

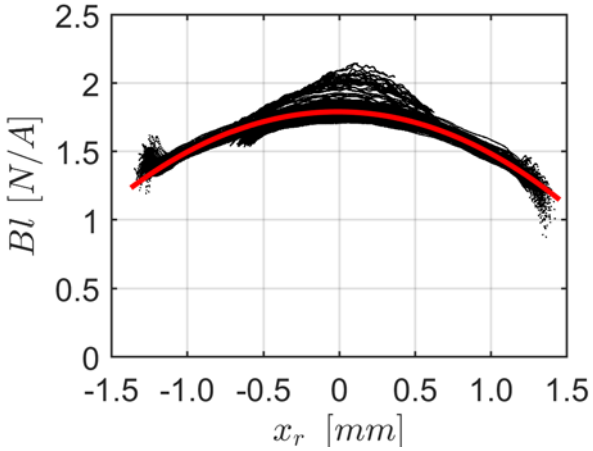

Figure 15: Model identification of the transduction factor; experimental data (black dots); fitted curve (red solid line).

The transduction coupling factor can be then written as,

$$Bl(x_r) = p_1 x_r^3 + p_2 x_r^2 + p_3 x_r + p_4, \tag{22}$$

where the parameters appearing in equation (22) are $p_1 = -300\ kN/Am^2$, $p_2 = -6.5\ N/Am$ and $p_3 = 1.8\ N/A$.

6. Modelling and simulation

In order to compare the dynamic behaviour of the nonlinear actuator with its underlying linear model, a numerical analysis is carried out. The experimental investigation presented in section 5 allows obtaining an accurate nonlinear lumped parameter model of the inertial actuator. The model we consider for the numerical analysis is the one shown in Figure 8, where the damping restoring force is given by equation (21), the elastic restoring force is given by the piecewise linear model of equation (20) and the transduction factor and all the other parameters are given by the linear model parameters of Table 1. The numerical analysis is performed considering the actuator in blocked base configuration ($x_b = 0$) whilst excited by the current flowing through the coil. Considering these assumptions, the equation of motion (14) can be solved in time domain via numerical integration. In this paper the Newmark integration method is used [52] with a sampling frequency $f_s = 10\ kHz$. Figure 16 shows the response of the proof mass to a sine sweep up (black line) and down (grey line) current excitation from 5 to 25 Hz at 1 Hz/min for $I_a = 0.1\ A$. The simulated response is limited by a maximum displacement until it jumps to the underlying linear response. A different approach to solve the nonlinear problem is using the harmonic balance method (HBM), which permits to find the periodic solution of equation (14). The method is explained in detail by Detroux *et al.* in [53] where the periodic solution has been approximated considering several harmonics in the response signal. In fact, to better understand the nonlinear behaviour of the stroke limited inertial actuator, the computation of higher order nonlinear frequency response curves is required, since the non-smooth nonlinearity activates higher harmonics. Simulation analysis involving the computation of periodic solutions are performed using the NI2D® software for this study [51]. The mathematical derivation of this approach can be found in [49, 53, 54]. Figure 16 shows the comparison between the nonlinear frequency response curve (NFRC) shown with the red dash-dotted line and the time domain simulation solved with Newmark method under the same excitation scenario. In this case, the response was computed up to the 5th harmonic. Assuming that the simulation in time domain is correct, it can be observed that the HBM is capable to fully predict the amplitude of the nonlinear response. Moreover, the bifurcation points predicted by the HBM correspond to the jump frequencies of the time domain analysis. It should be noted that for frequencies between 12.5 and 14.5 Hz the HBM gives three coexisting solutions. The middle branch is an unstable solution for the proof mass motion. The inertial actuator response stabilises on the upper or lower branch depending only on the initial conditions for a given level of excitation (level of the input current).

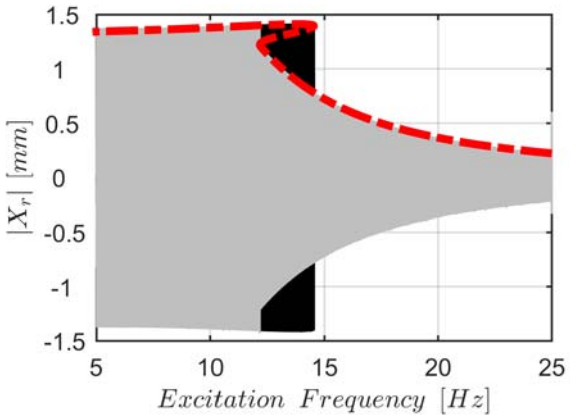

Figure 16: Comparison of the Newmark solution via integration of the equation of motion and the HBM. Solid black line for the Newmark sweep-up solution; solid grey line for the Newmark sweep-down solution; and dash dotted red line for the HBM solution.

The basins of attraction for the NFRC of Figure 16 at four different frequencies are shown in Figure 17 using the global analysis method [46]. In this figure, the state space mapping of the initial conditions that cause the system to stabilise on each branch of the NFRC is shown. In particular, the red circles represent the solutions that stabilise on the upper branch, whereas the white circles represent the solutions that stabilise on the lower branch. Figure 17(a) shows the basins of attraction at

12 Hz. At this frequency, the only solution is the upper branch. Shifting the frequency to 13 Hz causes both the attractors competing for the solution, as shown in Figure 17(b). At this frequency, the solution is more likely to stabilise on the upper branch. It can be seen that the initial condition on the velocity has a major influence on the solution, whereas being almost independent of the initial condition for the displacement. At 14 Hz the basins of attraction of the upper branch become less dominant, as shown in Figure 17(c). Ultimately, at 15 Hz all the initial conditions lead to the unique solution of the lower branch, as shown in Figure 17(d).

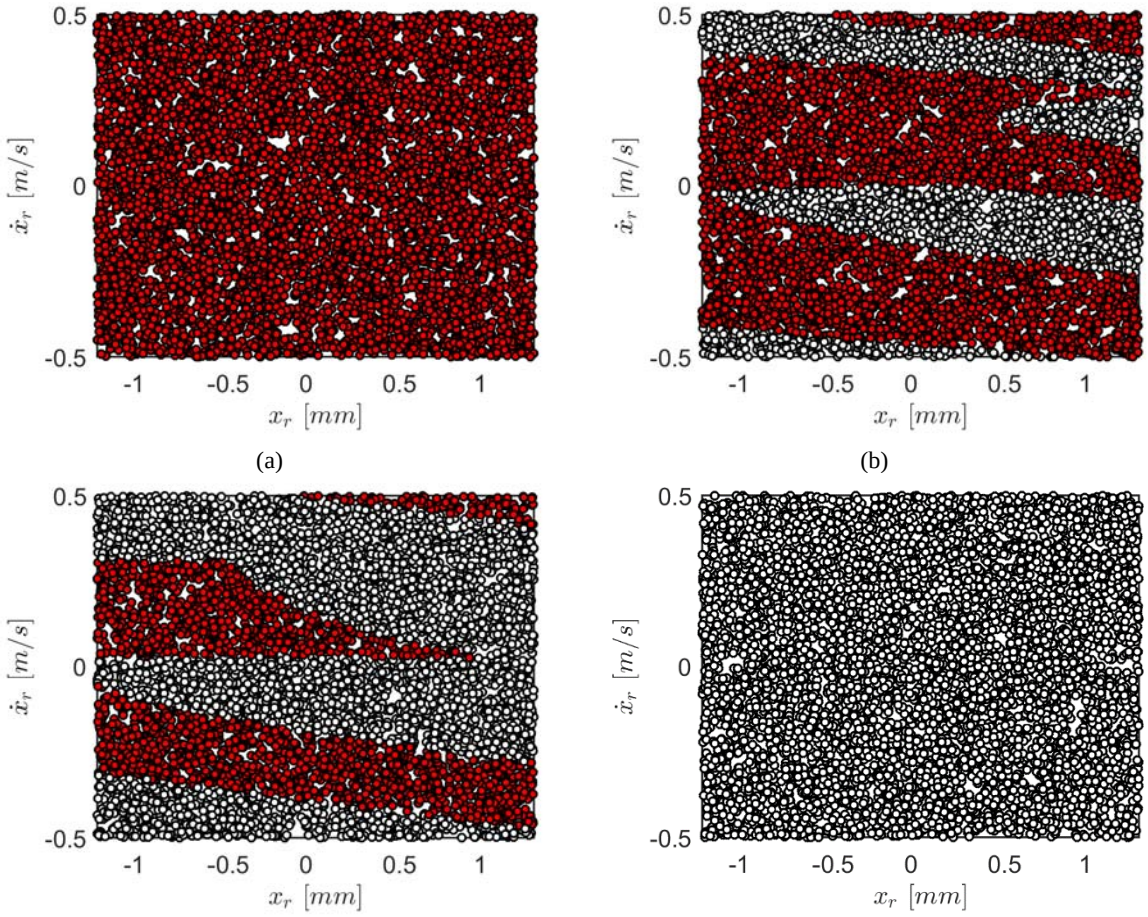

Figure 17: Basins of attraction for the NFRC of Figure 16: (a) 12 Hz; (b) 13 Hz; (c) 14 Hz; (d) 15 Hz; initial conditions that stabilises on the upper branch are displayed with red circles, initial conditions that stabilises on the lower branch are displayed with white circles.

The numerical analysis enables to test the actuator from low to very high level of excitation without destroying the actuator. Figure 18 shows a comparison between the NFRCs (black solid line) at increasing level of excitation, from 25 mA to 162.5 mA each simulation increasing of 12.5 mA. It can be observed that for the three lowest level of excitation the proof mass displacement do not exceed the stroke limits, hence the system is within its linear range and the NFRCs are effectively FRFs.

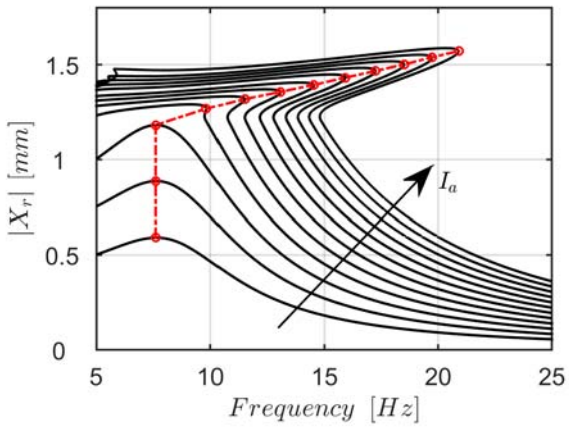

Figure 18: Linear FRFs and nonlinear frequency response functions for increasing excitation levels (solid black line); actuator's resonance frequency (red circles) and backbone curve (red dash dotted line).

The resonance frequency of the inertial actuator is invariant until the actuator encounters the nonlinearity. Increasing the input current the response becomes nonlinear with the nonlinear resonance frequency shifting monotonically towards higher frequencies, as shown in Figure 18 with the red circles connected with the red dash dotted line. However, the amplitude of the resonance peaks for the nonlinear system are proportionally lower than the resonance peak of the underlying linear system. This results in the NFRCs becoming particularly skewed towards higher frequency with respect to the linear FRFs. The values of the response are seen to be larger than the stroke length for certain value of the excitation. This is due to the finite stiffness of the end stops and to the excitation level that is larger than the one used in the experimental investigation. A comparison between the linear and nonlinear resonance frequency can be done in terms of the amplitude of either the response or the excitation. A simple, but straightforward study is to apply the HBM to equation (14) with a single harmonic approximation [49]. The equation of motion (14) is linearised for a given excitation, thus the restoring force is written as,

$$f_{RF}(x_r) \simeq K_{eq}(\omega, X_r)x_r, \tag{23}$$

where $K_{eq}(\omega, X_r)$ is an equivalent stiffness for a given operating condition. Harmonic balance is applied expanding a Fourier series for equation (20) and imposing a harmonic solution for the proof mass displacement. Noting that the restoring force is an odd function results in,

$$K_{eq}(\omega, X_r) = \frac{1}{\pi}\int_0^{2\pi} f_{RF}(X_r \sin(\omega t)) \sin(\omega t)\, \mathrm{d}\omega t, \tag{24}$$

which gives the mean value of the stiffness over one cycle of certain amplitude. Simplifying equation (24) considering equation (20), the equivalent stiffness can be written as,

$$K_{eq}(\omega, X_r) = k_p + \frac{(k_{sat}-k_p)}{\pi}\left[\pi - 2\arcsin\left(\frac{x_0}{X_r}\right) - 2\frac{x_0}{X_r^2}\sqrt{X_r^2 - x_0^2}\right], \tag{25}$$

which is also known as describing function of the nonlinearity [49, 55].The change of the nonlinear resonance frequency with the amplitude of oscillation can be normalised to the resonance frequency of the underlying linear system [49]. Hence, a nondimensional parameter can be introduced as,

$$\beta = \frac{\omega_{res,NL}^2}{\omega_p^2} = \frac{K_{eq}(\omega, X_r)}{k_p}, \tag{26}$$

where $\omega_{res,NL}$ is the resonance frequency of the nonlinear system. Equation (26) is plotted in Figure 19(a) considering equation (25) and the values in Table 1. This figure shows a direct comparison between the nonlinear resonance frequency (red dash dotted line) and the underlying liner resonance frequency (black solid line) with respect to the amplitude of the proof mass displacement. Figure 19(b) instead, shows the comparison between the linear and nonlinear resonance frequencies with respect to the amplitude of the excitation.

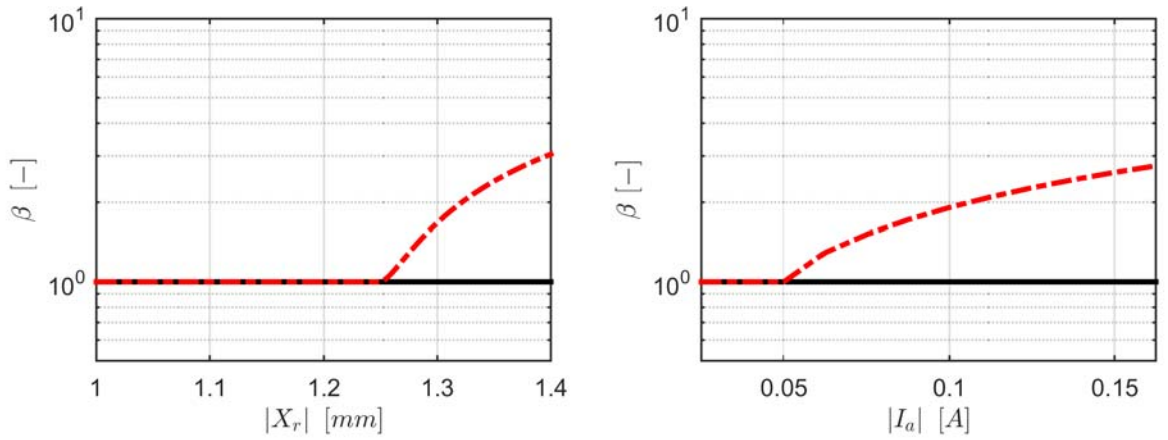

(a) (b)

Figure 19: Variation in the resonance frequency with: (a) amplitude of oscillation; (b) amplitude of excitation. Black solid line for the underlying linear model and red dash-dotted line for the nonlinear model.

This corresponds to the backbone curve of Figure 18. In both Figure 19(a,b), the nonlinear resonance frequency is invariant until the inertial actuator enters the nonlinear region, and then increases consistently. This can be a threat when the inertial actuator is used in a velocity feedback loop, since an increase in the actuator's resonance frequency can lead to a decrease of the stability margin of the controller.

7. Conclusions

In this paper an experimental investigation on the nonlinear behaviour of an inertial actuator has been presented. Firstly, the experimental set-up has been described, which involved the base excitation and base blocked experiments. Secondly, the underlying linear parameters have been identified using the transmissibility, the mechanical and the electrical impedances of the inertial actuator. Then, the nonlinear behaviour of the inertial actuator has been investigated, starting from the detection of the nonlinearity, its characterisation and the identification of the nonlinear parameters to the numerical analysis. The nonlinear characterisation analysis led to a piecewise linear model of the elastic restoring force, a linear model of the damping restoring force and a polynomial quadratic model of the transduction factor. The nonlinear parameters have been identified using the restoring force method. Finally, the numerical analysis using the harmonic balance method has shown that the hardening stiffness nonlinearity increases the resonance frequency of the actuator significantly. This causes a reduction in the stability margin of velocity feedback controllers. Future work may concentrate into developing control strategies that accounts for the actuator nonlinearity by maximising the stability of the control system yet maintaining the vibration reduction performance provided by the velocity feedback loop.

Acknowledgements

The authors gratefully acknowledge the European Commission for its support of the Marie Curie program through the ITN ANTARES project (General Agreement 606817). The results presented in this paper were partly obtained using the NI2D software developed by the Space Structures and Systems Laboratory (S3L), University of Liège. The first author acknowledges the Adaptronik group of the Fraunhofer LBF for their collaboration during a visiting research period.

Appendix A: LBF inertial actuator

The same nonlinear identification methodology was applied to 10 others different actuators. In this appendix, the results of the experimental investigation are shown for one of those actuators. Figure A.1 shows a prototype inertial actuator developed by Fraunhofer LBF (Darmstadt, Germany), which was characterised during a test campaign at their laboratories.

Figure A.1: Picture of the Fraunhofer LBF inertial actuator.

The measured and identified mechanical impedances in open circuit and closed circuit are shown in Figure A.2(a) and (b), respectively. Figure A.3(a) shows the measured and identified transmissibility measured for the base excitation scenario, whereas Figure A.3(b) shows the transmissibility with respect to the input current for the blocked base experiment. Figure A.4(a) shows the measured and identified transmissibility with respect to the input voltage for the base blocked scenario. The measured electrical impedance is shown in Figure A.4(b) with the black solid line. The ideal inductance model (blue dash dotted line) and the LR-2 model (red dotted line) given by equation (1) were fitted to the data. It can be seen that the LR-2 model of the electrical port gives much better agreement with the measured data.

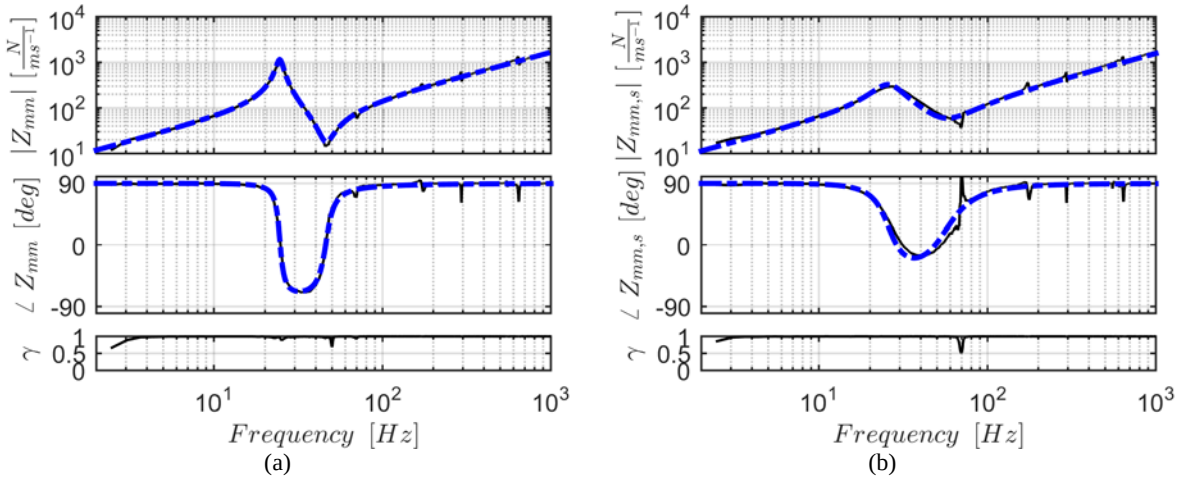

(a) (b)

Figure A.2: Magnitude, phase and coherence of the measured and averaged FRFs per unit input (black solid line) and identified model (blue dashed line): (a) mechanical impedance in open circuit configuration; (b) mechanical impedance in shunted circuit configuration.

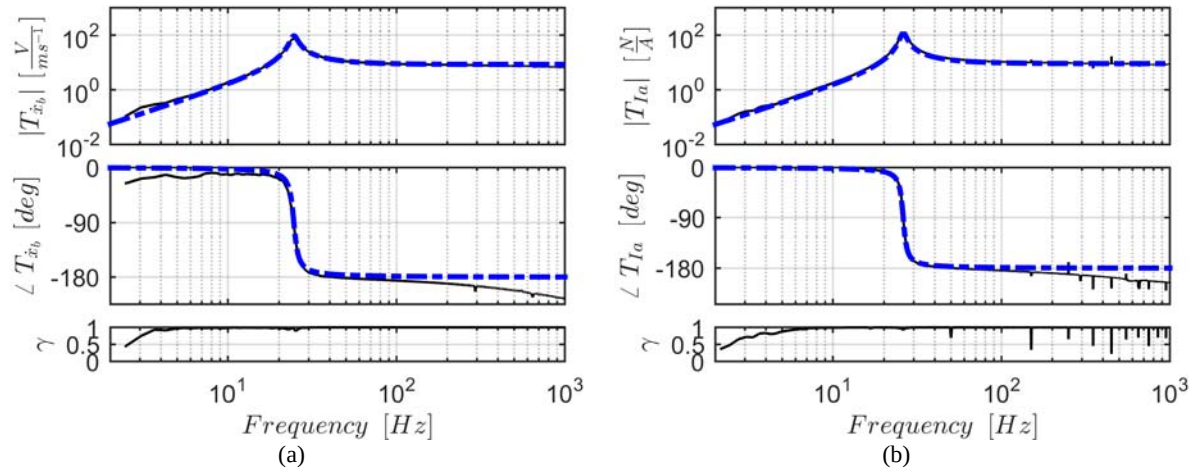

(a) (b)

Figure A.3: Magnitude, phase and coherence of the measured and averaged FRFs per unit input (black solid line) and identified model (blue dashed line): (a) transmissibility for the base excitation experiment; (b) transmissibility for the base blocked current excitation experiment.

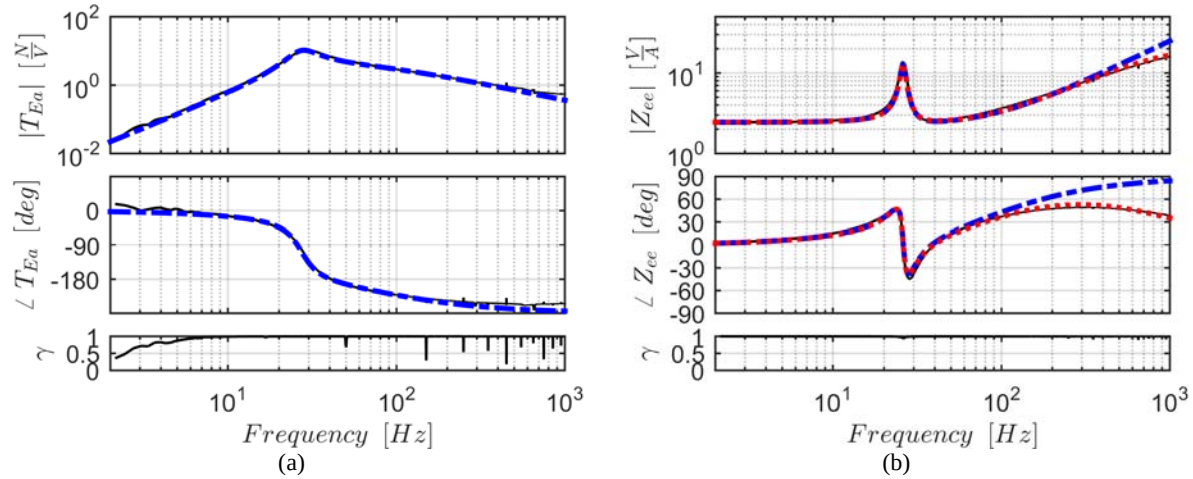

(a) (b)

Figure A.4: Magnitude, phase and coherence of the measured and averaged FRFs per unit input (black solid line) and identified model (blue dashed line): (a) transmissibility for the base blocked voltage excitation experiment; (b) electric impedance in blocked base configuration considering an ideal inductance model (blue dashed line) and a LR-2 model for the inductance losses (red dotted line).

The actuator was then tested with the same methodology explained in section 5. The results of the nonlinearity identification are shown in Figure A.5. In particular Figure A.5(a) displays the experimental data points of the restoring force versus the state space. Figure A.5(b) shows the experimental data points of the elastic restoring force and the fitted model. It can be seen that the elastic restoring force behaves linearly even for high amplitude oscillations, until the proof mass reaches one end stop. Hence, the fitted model is piecewise linear with the discontinuity point at the location of the stroke limit. Figure A.5(c) shows the scattered data point of the damping restoring force and the identified model. The behaviour is weakly nonlinear and it has been identified as polynomial of the third order. The scattered data plot of the transduction factor versus the displacement is shown in Figure A.5(d). Its behaviour is given by a third order polynomial function, which is asymmetric with respect to the proof mass resting position. In fact, the peak in the transduction coupling factor is reached for negative displacements, whereas positive displacements lead to a significant decrease.

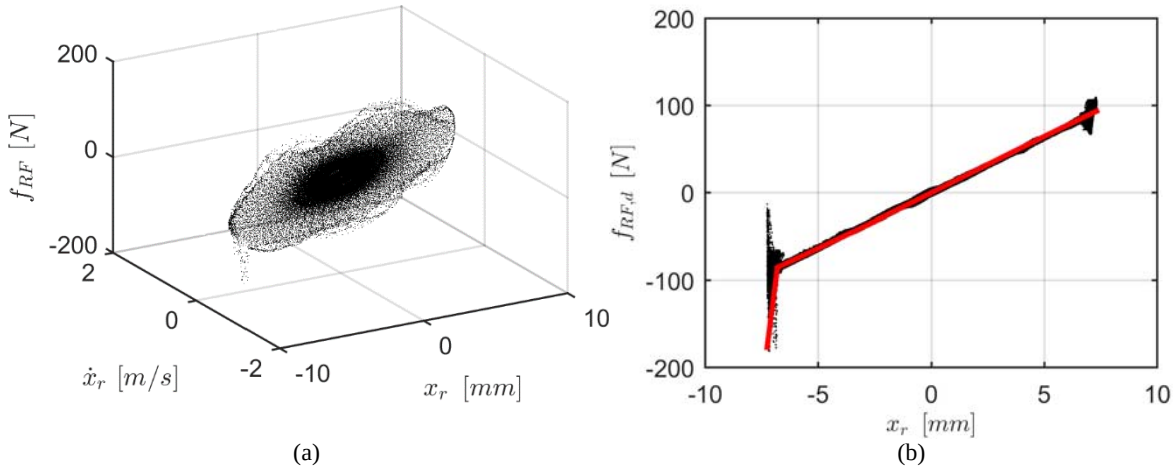

(a) (b)

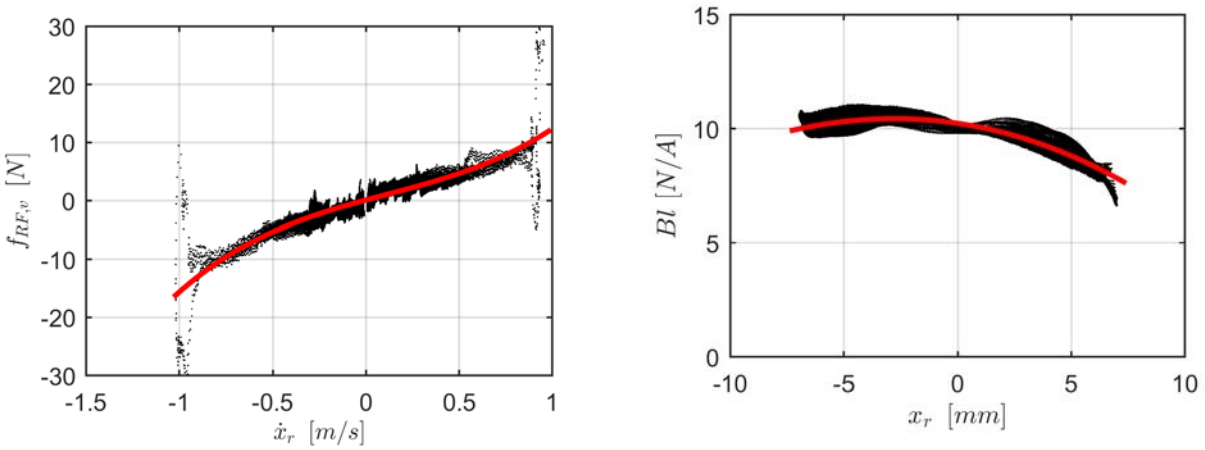

(c) (d)

Figure A.5: Restoring force data points: (a) 3D restoring force in the phase space; (b) elastic restoring force; (c) damping restoring force; (d) transduction factor; experimental data (black dots); fitted curve (red solid line).

Appendix B: Tectonic Elements TEBM inertial actuator

Another application example of the identification methodology is given in this appendix on a different actuator. Figure B.1 shows a commercial Tectonic Elements TEBM46C20N-4B audio speaker, which can be used as inertial actuator. The measured and identified mechanical impedances in open circuit and closed circuit are shown in Figure B.2(a) and (b), respectively. Figure B.3(a) shows the measured and identified transmissibility measured for the base excitation scenario, whereas Figure B.3(b) shows the transmissibility with respect to the input current for the blocked base experiment. Figure B.4(a) shows the measured and identified transmissibility with respect to the input voltage for the base blocked scenario. The measured electrical impedance is shown in Figure B.4(b) with the black solid line. The ideal inductance model (blue dash dotted line) and the Leach model (red dotted line) given by equation (C3) were fitted to the data. It can be seen that the Leach model of the electrical port gives much better agreement with the measured data.

Figure B.1: Picture of the Tectonic Elements TEBM46C20N-4B audio speaker.

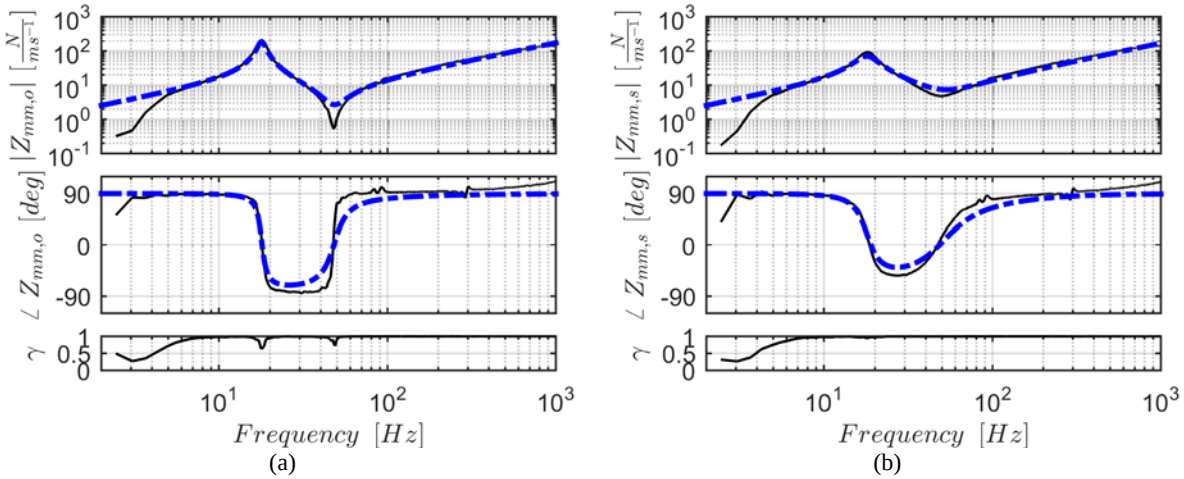

(a) (b)

Figure B.2: Magnitude, phase and coherence of the measured and averaged FRFs per unit input (black solid line) and identified model (blue dashed line): (a) mechanical impedance in open circuit configuration; (b) mechanical impedance in shunted circuit configuration.

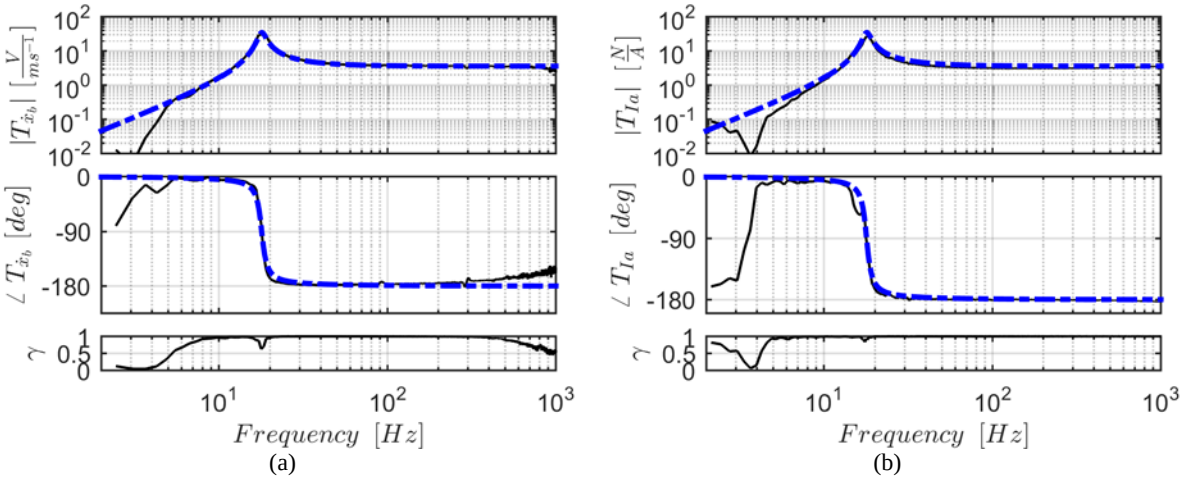

(a) (b)

Figure B.3: Magnitude, phase and coherence of the measured and averaged FRFs per unit input (black solid line) and identified model (blue dashed line): (a) transmissibility for the base excitation experiment; (b) transmissibility for the base blocked current excitation experiment.

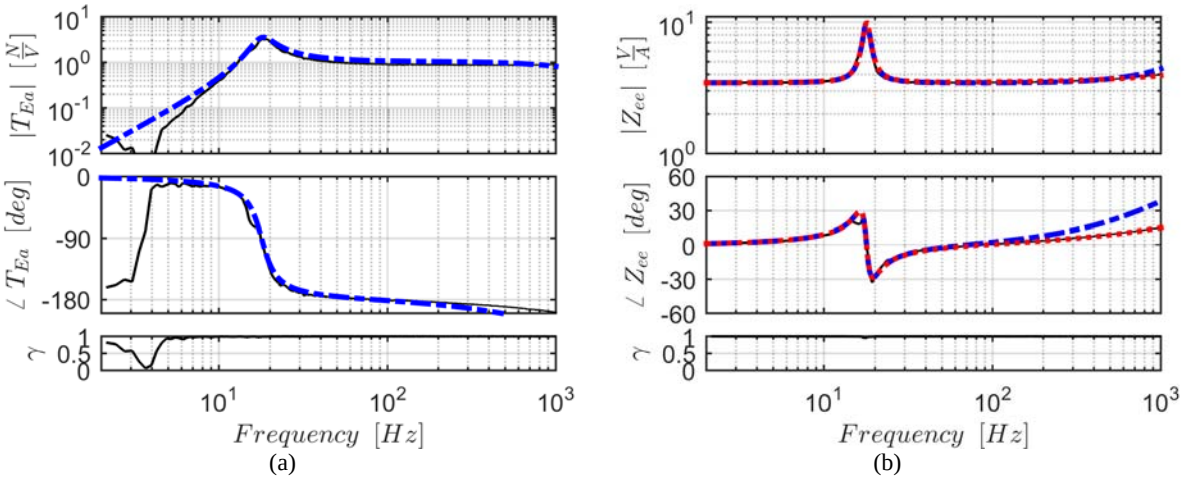

(a) (b)

Figure B.4: Magnitude, phase and coherence of the measured and averaged FRFs per unit input (black solid line) and identified model (blue dashed line): (a) transmissibility for the base blocked voltage excitation experiment; (b) electric impedance in blocked base configuration considering an ideal inductance model (blue dashed line) and a Leach model for the inductance losses (red dotted line).

The actuator was then tested with the same methodology explained in section 5. The results of the nonlinearity identification are shown in Figure B.5. In particular Figure B.5(a) displays the experimental data points of the restoring force versus the state space. Figure B.5(b) shows the experimental data points of the elastic restoring force and the fitted model. It can be seen that the elastic restoring force behaves nonlinearly and asymmetrically with respect to the resting position of the proof mass. Hence, the fitted model is piecewise linear with the discontinuity point at displacement zero. Figure B.5(c) shows the scattered data point of the damping restoring force and the identified model. The behaviour is highly nonlinear and it has been identified as polynomial of the third order. In particular, for positive velocities the damping restoring force is almost constant. This can be do to the friction between the coil support and the proof mass. The scattered data plot of the transduction factor versus the displacement is shown in Figure B.5(d). Its behaviour is given by a linearly decreasing function. In fact, for negative displacements the transduction factor keeps increasing without reaching a peak, whereas for positive displacements the coil decouples with the magnet and the transduction factor decreases significantly.

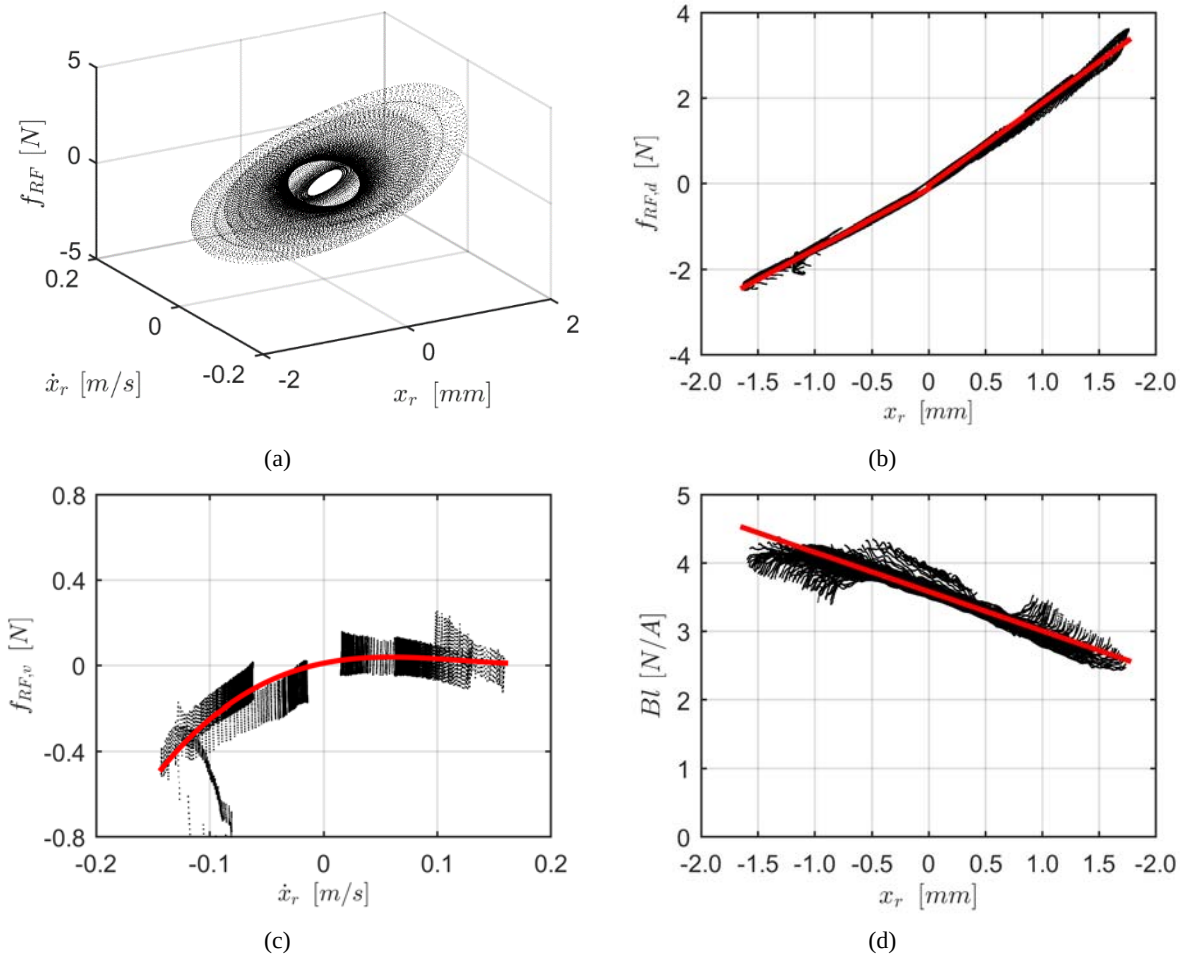

Figure B.5: Restoring force data points: (a) 3D restoring force in the phase space; (b) elastic restoring force; (c) damping restoring force; (d) transduction factor; experimental data (black dots); fitted curve (red solid line).

Appendix C: Inductance losses models

The LR-2 model of the inductance losses is not the only one that aims to describe this behaviour. In fact, further investigations showed the development of different linear models to describe the inductance losses due to the eddy currents in the iron pole. In fact, J. Vanderkooy [37] derived a mathematical formulation that models the behaviour of the voice coil as a series resistor and semi-inductor, which has an electrical impedance

$$Z_L(j\omega) = K\sqrt{j\omega}, \tag{C1}$$

as shown in Figure 20(b). This model requires the identification of one parameter. Subsequently, J. R. Wright proposed a model with separated power functions for the real and imaginary part of the electrical impedance [56]. That is,

$$Z_L(j\omega) = K_r\omega^{X_r} + jK_i\omega^{X_i}. \tag{C2}$$

This model cannot be represented by an equivalent electrical circuit and it requires the identification of four parameters. A similar model was developed by W. M. Leach [42], where the electrical impedance takes the form,

$$Z_L(j\omega) = K(j\omega)^n, \tag{C3}$$

which requires the identification of two parameters. W. M. Leach also proposed a model described by a series effective inductance and resistance in which the inductance and resistance vary with frequency [57], as shown in Figure 20(c). Hence, the electrical impedance of the effective inductance model can be written as,

$$Z_L(j\omega) = L_{eff}(\omega)j\omega + R_{eff}(\omega), \tag{C4}$$

which requires a large amount of parameters: two for each frequency point. Any of these models can be used and in fact, it has been observed that the choice of each model strongly depends on the actuator design.

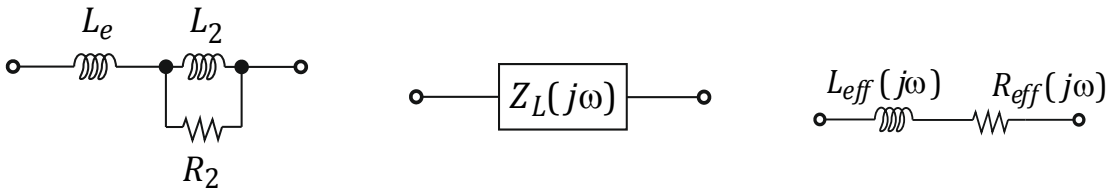

(a) (b) (c)

Figure 20: Topology of the electrical impedance considering the effect of the inductance losses due to eddy currents: (a) LR-2 model; (b) Wright and Leach frequency dependent model; (c) effective inductance model.

Table 4: Identified parameters of the lossy inductor using a Leach model [42], as in equation (C3).

Parameter	Semi-inductance	Frequency exponent
Symbol	K	n
Value	$4.5*10^{-4}$	0.85
Units	-	-

References

[1] L. Meirovitch, Dynamics and control of structures, John Wiley & Sons, New York, 1990.
[2] C.C. Fuller, S.J. Elliott, P.A. Nelson, Active control of vibration, Academic Press, 1996.
[3] S.J. Elliott, Signal processing for active control, Academic press, 2001.
[4] D.J. Inman, Vibration with control, John Wiley & Sons, 2006.
[5] F. Fahy, P. Gardonio, Sound and structural vibration: radiation, transmission and response, 2nd ed., Elsevier Science, 2007.
[6] D.J. Wagg, S.A. Neild, Nonlinear vibration with control: for flexible and adaptive structures, Springer, the Netherlands, 2010.
[7] A. Preumont, Vibration control of active structures: an introduction, Springer, the Netherlands, 2011.

[8] P. Gardonio, C.G. Díaz, Downscaling of proof mass electrodynamic actuators for decentralized velocity feedback control on a panel, Smart Materials and Structures, 19 (2010).
[9] J. Rohlfing, P. Gardonio, S.J. Elliott, Base impedance of velocity feedback control units with proof-mass electrodynamic actuators, Journal of Sound and Vibration, 330 (2011) 4661-4675.
[10] J. Rohlfing, S.J. Elliott, P. Gardonio, Feedback compensator for control units with proof-mass electrodynamic actuators, Journal of Sound and Vibration, 331 (2012) 3437-3450.
[11] C.G. Díaz, C. Paulitsch, P. Gardonio, Smart panel with active damping units. Implementation of decentralized control, J. Acoust. Soc. Am., 124 (2008) 898-910.
[12] C.G. Díaz, C. Paulitsch, P. Gardonio, Active damping control unit using a small scale proof mass electrodynamic actuator, J. Acoust. Soc. Am., 124 (2008) 886-897.
[13] C. Paulitsch, P. Gardonio, S.J. Elliott, Active vibration control using an inertial actuator with internal damping, J. Acoust. Soc. Am., 119 (2006) 2131-2140.
[14] S. Camperi, M. Ghandchi Tehrani, S.J. Elliott, Experimental maximisation of the power absorbed by an inertial actuator for structural vibration control, International Congress on Sound and Vibration, London, UK, 2017.
[15] W.L. Hallauer, S.E. Lamberson, Experimental active vibration damping of a plane truss using hybrid actuation, 30th Structures, Structural Dynamics and Materials Conference, AIAA, Mobile, AL, U.S.A., 1989, pp. 80-90.
[16] I.M. Díaz, E. Pereira, M.J. Hudson, P. Reynolds, Enhancing active vibration control of pedestrian structures using inertial actuators with local feedback control, Engineering Structures, 41 (2012) 157-166.
[17] P. Gardonio, Review of active techniques for aerospace vibro-acoustic control, Journal of aircraft, 39 (2002) 206-214.
[18] C.R. Fuller, J.D. Jones, Experiments on reduction of propeller induced interior noise by active control of cylinder vibration, Journal of Sound and Vibration, 112 (1987) 389-395.
[19] C.G. Díaz, P. Gardonio, Feedback control laws for proof-mass electrodynamic actuators, Smart Materials and Structures, 16 (2007) 1766-1783.
[20] S.J. Elliott, L. Benassi, M.J. Brennan, P. Gardonio, X. Huang, Mobility analysis of active isolation systems, Journal of Sound and Vibration, 271 (2004) 297-321.
[21] S.J. Elliott, M. Serrand, P. Gardonio, Feedback stability limits for active isolation systems with reactive and inertial actuators, J. Vib. Acoust.-Trans. ASME, 123 (2001) 250-261.
[22] O.N. Baumann, S.J. Elliott, Destabilization of velocity feedback controllers with stroke limited inertial actuators, The Journal of the Acoustical Society of America, 121 (2007) EL211-EL217.
[23] O.N. Baumann, S.J. Elliott, The stability of decentralized multichannel velocity feedback controllers using inertial actuators, The Journal of the Acoustical Society of America, 121 (2007) 188-196.
[24] L.I. Wilmshurst, Analysis and control of nonlinear vibration in inertial actuators, Institute of Sound and Vibration Research, University of Southampton, Southampton, UK, 2015.
[25] L.I. Wilmshurst, M. Ghandchi Tehrani, S.J. Elliott, Nonlinear identification of proof-mass actuators accounting for stroke saturation, Proceedings of ISMA 2014: International Conference on Noise and Vibration Engineering, Leuven, Belgium, 2014, pp. 209-223.
[26] L.I. Wilmshurst, M. Ghandchi Tehrani, S.J. Elliott, Preventing of stroke saturation in inertial actuators using a detection scheme, The 21st International Congress on Sound and Vibration (ICSV21), Beijing, China, 2014.
[27] M. Dal Borgo, M. Ghandchi Tehrani, S.J. Elliott, Dynamic analysis of two nonlinear inertial actuators in active vibration control, 27th International Conference on Noise and Vibration Engineering (ISMA2016), Leuven, Belgium, 2016.
[28] M. Dal Borgo, M. Ghandchi Tehrani, S.J. Elliott, Nonlinear control and stability analysis of a stroke limited inertial actuator in velocity feedback, 9th European Nonlinear Dynamics Conference (ENOC2017), Budapest, Hungary, 2017, pp. 1-10.
[29] M. Dal Borgo, M. Ghandchi Tehrani, S.J. Elliott, Dynamic analysis of nonlinear behaviour in inertial actuators, 13th International Conference on Motion and Vibration Control (MOVIC 2016) and the 12th International Conference on Recent Advances in Structural Dynamics (RASD 2016), Journal of Physics Conference Series, Southampton, UK, 2016, pp. 012027.

[30] L.I. Wilmshurst, M. Ghandchi Tehrani, S.J. Elliott, Nonlinear vibrations of a stroke-saturated intertial actuator, 11th International Conference on Recent Advances in Structural Dynamics (RASD 2013), Pisa, Italy, 2013.
[31] H. Politansky, W.D. Pilkey, Suboptimal feedback vibration control of a beam with a proof-mass actuator, J. Guid. Control Dyn., 12 (1989) 691-697.
[32] J. Scruggs, D. Lindner, Optimal sizing of a proof-mass actuator, 40th Structures, Structural Dynamics, and Materials Conference, American Institute of Aeronautics and Astronautics, St. Louis, MO USA, 1999.
[33] Micromega Dynamics, Active damping devices and inertial actuators, 2016.
[34] Micromega Dynamics, Inertial actuator - operation and maintenance manual. Prepared for Institute of Sound and Vibration Research, University of Southampton, 2005.
[35] M. Dodd, W.J. Klippel, J. Oclee-Brown, Voice coil impedance as a function of frequency and displacement, 117th Audio Engineering Society Convention, San Francisco, CA, USA, 2004.
[36] W.J. Klippel, U. Seidel, Fast and accurate measurement of linear transducer parameters, 110th Audio Engineering Society Convention, Amsterdam, The Netherlands, 2001.
[37] J. Vanderkooy, A model of loudspeaker driver impedance incorporating eddy currents in the pole structure, Journal of the Audio Engineering Society, 37 (1989) 119-128.
[38] A.N. Thiele, Loudspeakers in vented boxes: Part 1, Journal of the Audio Engineering Society, 19 (1971) 382-392.
[39] A.N. Thiele, Loudspeakers in vented boxes: Part 2, Journal of the Audio Engineering Society, 19 (1971) 471-483.
[40] F.V. Hunt, Electroacoustics: the analysis of transduction, and its historical background, Harvard University Press, Cambridge, 1954.
[41] S.H. Crandall, Dynamics of mechanical and electromechanical systems, McGraw-Hill, New York, 1968.
[42] W.M. Leach, Loudspeaker voice-coil inductance losses: circuit models, parameter estimation, and effect on frequency response, Journal of the Audio Engineering Society, 50 (2002) 442-450.
[43] C. Paulitsch, P. Gardonio, S.J. Elliott, P. Sas, R. Boonen, Design of a lightweight, electrodynamic, inertial actuator with integrated velocity sensor for active vibration control of a thin lightly-damped panel, in: P. Sas, M. De Munck (Eds.) Proceedings of ISMA 2004: International Conference on Noise and Vibration Engineering, Katholieke Universiteit Leuven, Leuven, Belgium, 2005, pp. 239-253.
[44] C. Paulitsch, Vibration control with electrodynamic actuators, Institute of Sound and Vibration Research, University of Southampton, 2005.
[45] G. Kerschen, K. Worden, A.F. Vakakis, J.-C. Golinval, Past, present and future of nonlinear system identification in structural dynamics, Mech Syst Signal Pr, 20 (2006) 505-592.
[46] J.-P. Noël, G. Kerschen, Nonlinear system identification in structural dynamics: 10 more years of progress, Mech Syst Signal Pr, 83 (2017) 2-35.
[47] J.-P. Noël, L. Renson, G. Kerschen, Complex dynamics of a nonlinear aerospace structure: experimental identification and modal interactions, Journal of Sound and Vibration, 333 (2014) 2588-2607.
[48] K. Worden, Data-processing and experiment design for the restoring force surface method, part 1: integration and differentiation of measured time data, Mech Syst Signal Pr, 4 (1990) 295-319.
[49] K. Worden, G.R. Tomlinson, Nonlinearity in structural dynamics: detection, identification and modelling, Institute of Physics, Bristol, UK, 2000.
[50] D. Shmilovitz, On the definition of total harmonic distortion and its effect on measurement interpretation, IEEE Trans. Power Deliv., 20 (2005) 526-528.
[51] nolisys, Nonlinear identification to design software (NI2D®), 2017.
[52] M.M.I. Baig, T. Grätsch, Recommendations for practical use of numerical methods in linear and nonlinear dynamics, Simpson Gumpertz and Heger, Inc, Waltham, MA, USA, 2005.
[53] T. Detroux, L. Renson, L. Masset, G. Kerschen, The harmonic balance method for bifurcation analysis of large-scale nonlinear mechanical systems, Comput. Meth. Appl. Mech. Eng., 296 (2015) 18-38.

[54] A. Pavlov, N. van de Wouw, H. Nijmeijer, Frequency response functions and Bode plots for nonlinear convergent systems, Proceedings of the 45th IEEE Conference on Decision and Control, Ieee, San Diego, CA, USA, 2006, pp. 3765-3770.
[55] J.E. Gibson, Nonlinear automatic control, 1963.
[56] J.R. Wright, An empirical model for loudspeaker motor impedance, Journal of the Audio Engineering Society, 38 (1990) 749-754.
[57] W.M. Leach, Introduction to electroacoustics and audio amplifier design, Kendall/Hunt Publishing Company, 2003.